An Investigation of the $Cl^{-}\cdots CO$ and $Br^{-}\cdots CO$ van der Waals Clusters with Anion Photoelectron Spectroscopy and *ab initio* Calculations

Kim Lapere

Signed Statement

I certify that the substance of this thesis has not previously been submitted for any degree or diploma and is not currently being submitted for any degree or diploma.

I certify that, to the best of my knowledge, any help received in preparing this thesis, and sources used, have been acknowledged in the thesis.

_____

Kim Lapere, October 2009

Summary

Anion photoelectron spectroscopy is a technique that gives detailed information about the energy levels of neutral species by photodetaching an electron from the anion species. It is often compared with theoretical results, as has been demonstrated here. From the predicted and experimental spectra data pertinent to reaction kinetics can be obtained. These are important in areas of research such as atmospheric chemistry, where the relevance of this project lies.

This year preliminary spectra have been recorded on the newly completed Time of Flight Mass Spectrometer coupled to a PhotoElectron Spectrometer. Clusters involving carbon monoxide and the halogens chlorine and bromine have been explored.

The optimised geometries were determined to be strongly bent for the anion species and linear for the neutral species of both clusters. Potential energy surfaces in one and two-dimensions have been created, and the overlap of vibrational waveforms on the intermolecular stretch compared. These have provided Franck-Condon factors necessary to predict the most favourable transition between states.

Predicted spectra generated for each cluster from these *ab initio* calculations show agreeable structure to the recorded photoelectron spectra however the resolution of the apparatus requires further enhancement. The most favourable transition for both complexes from the anion species to the $^{2}\Sigma^{+}$ electronic state of the neutral species was determined to be $0 \leftarrow\!\!- 0$ for both basis sets.

Acknowledgements

It goes without saying that the single person every honours student cannot complete their thesis without, is their supervisor. But often it is much more than simply supervising they do. Thank you, Duncan Wild for answering each and every question I had, but also for all the side-projects, you made it so fun I didn't even realise it was hard work. I have learnt so much more than what is contained in these pages.

Many parts of the TOF-PES would not be running today without the dedicated work of the staff from the Mechanical Workshop of the School of Biomedical, Biomolecular and Chemical Sciences: Nigel Hamilton, Andrew Sawyer, Damien Bainbridge and Trevor Franklin. Your help has made this project run smoothly.

Many thanks to WASP (UWA), NCI and iVEC facilities for permitting the use of their supercomputers. This must also be extended to Prof. Allan McKinley, for the lending of his lab computers.

Thank you again Prof. Allan McKinley for the kind use of the laser!

I was honoured to receive the Raoul Robellaz Kahan scholarship this year, and would like to thank Miss Jean Kahan for providing this chemistry scholarship in the name of her father.

Lastly thanks to the friends and family I cannot do without, and who give me the strength to carry on: Michael Pearce, Nilukshi Ranwala, and all the other late-nighters! You guys made this year cooler.

Table of Contents

Signed Statement i

Summary ii

Acknowledgements iii

Table of Contents iv

List of Figures vii

List of Tables x

List of Abbreviations x

1. Introduction 1

1.1. Project aims 1

1.2. Intermolecular interactions 2

1.3. Potential energy surfaces 2

1.4. Atmospheric chemistry 3

1.4.1. Ozone 4

1.4.2. Carbon monoxide 5

1.4.3. Halogens 6

1.4.4. Extraterrestrial systems 7

1.5. Cluster science 8

1.6. Photoelectron spectroscopy 9

1.6.1. The Photoelectric effect 9

1.6.2. Anion photoelectron spectroscopy 10

2. Method & materials 12

2.1. TOF-PES 12

2.2. Experimental method 14

2.2.1. Gas mixture for halide-carbon monoxide clusters 14

2.2.2. Making the anion clusters 15
2.2.3. Selecting the ion of interest, and slowing them down 17
2.2.4. Recording photoelectron spectra 18
2.2.5. Operating conditions 19
2.2.6. Timing scheme of pulses 21
2.3. Modifications to the TOF-PES 23
2.4. Theoretical methodology 28
3. Experimental results & discussion 31
3.1. Mass spectra 31
3.2. Photoelectron spectra 33
3.3. Improving the resolution 36
4. Theoretical results & discussion 37
4.1. Optimised geometries 38
4.2. 1D Potential energy slices 40
4.2.1. $\nu_{X\text{-}CO}$ stretch 40
4.2.2. ν_{CO} stretch 42
4.2.3. $\theta_{X\text{-}CO}$ bend 43
4.3. 2D Potential energy slices 45
4.3.1. Comparison with DFT methods 50
4.4. Predicted spectra 52
4.4.1. $Cl^{\cdots}CO$ 52
4.4.2. $Br^{\cdots}CO$ 55
5. Future work 57
6. Conclusion 60
7. Appendices 61
7.1. Appendix 1 61

7.2. Appendix 2 64

7.3. Appendix 3 64

7.4. Appendix 4 66

8. References 67

List of Figures

Figure 1 - A typical potential energy surface.[1] 3

Figure 2 - The temperature-altitude profile for the Earth's atmosphere on which the boundaries between the five different atmospheric layers are based on.[3] 4

Figure 3 – The photoelectric effect on solid potassium. Only photons with permissible energies will be absorbed, causing photoelectrons to be emitted with the excess energy being converted into kinetic energy.[11] 10

Figure 4 - The adiabatic electron affinity shown on an anion to neutral progression.[12] 11

Figure 5 - The time-of-flight mass spectrometer coupled to the photoelectron spectrometer in the Wild laboratory.[17] 12

Figure 6 – Schematic of the current laser setup. 14

Figure 7 – Schematic demonstrating the deflection of anions towards the time-of-flight tube using negatively charged plates. 16

Figure 8 – Schematic showing the path of ions and photoelectrons, with an inset of a detailed view of the bottleneck magnetic field produced to trap the photoelectrons. Courtesy of Quak[16] (top) and Dr D. Wild[17] (inset, orientated 90° CCW to the main figure). 18

Figure 9 – Typical background (red) for a photoelectron spectrum (black). 20

Figure 10 – Pulsing sequence for the operation of the TOF-PES. Taken from Quak.[16] 22

Figure 11 – Schematic of the knife-edges imposed on the orifice past the X-Y deflection plates. 23

Figure 12 – Photo of the laser safety enclosure box with the lids removed. 26

Figure 13 - The three vibrational modes possible for the three-atom system: two stretching and one bending, shown on the $Cl^{-\cdots}CO$ cluster. 1D potential energy scans involve

calculating the energy at the optimised geometry in multiple steps during one such mode. Jacobi coordinates system. 29

Figure 14 - The Franck-Condon principle[24] illustrating favoured electronic transitions between the vibrational states v = 0 and v = 2. 30

Figure 15 – A mass spectrum of bromide, chloride and their clusters with carbon monoxide. The chloride and bromide peaks are cut off (their intensities are close to 1 V) to show the weaker species. 31

Figure 16 - Larger clusters of bromide and chloride with carbon monoxide. Other species are also shown. 32

Figure 17 - The photoelectron spectra of ^{35}Cl and $^{35}Cl^{\cdots}CO$ at 90°. 33

Figure 18 - The photoelectron spectra of ^{79}Br and $^{79}Br^{\cdots}CO$. 34

Figure 19 – A more symmetrical distribution of photoelectrons is produced when the laser polarisation angle is parallel to the flight axis of the photoelectrons (i.e. at 0°). 35

Figure 20 – Using the ion decelerator to improve the resolution of photoelectron spectra 36

Figure 21 - The optimised geometry of the $Cl^{-\cdots}CO$ clusters: a) anion species and b) and c) the two neutral species. 38

Figure 22 - The optimised geometry of the $Br^{-\cdots}CO$ clusters: a) anion species and b) and c) the two neutral species. 38

Figure 23 - The $\nu_{X\text{-}CO}$ stretch for X = Cl (top), Br (bottom). The neutral species (right scale on the y-axis) have been referenced to the anion (left scale). 41

Figure 24 – A ν_{CO} stretch for $Cl^{-\cdots}CO$ (top) and $Br^{-\cdots}CO$ (bottom) clusters. The neutral species have been referenced to the anion's lowest energy. 42

Figure 25 - A $\theta_{X\text{-}CO}$ bend. Both neutral species (right scale) have been referenced to the anion (left scale). For the $Cl^{-\cdots}CO$ cluster the surface is symmetric at 180° as it shows the same position but mirrored. For the $Br^{\cdots}CO$ cluster both neutral species showed irregularities that require further investigation. 44

Figure 26 - A ‘slice’ of the 2D potential energy scan of the $Cl^{-}\cdots CO$ anion (top) and neutral (bottom). This slice was taken while maintaining a CO distance of 1.2 Å and scanning the $\nu_{Cl\text{-}CO}$ stretch and $\theta_{Cl\text{-}CO}$ bend. 47

Figure 27 - A ‘slice’ of the 2D potential energy scan of the Cl-CO anion (top) and neutral (bottom) calculated at MP2/aug-cc-pvtz (in GAMESS [21] for the neutral). This slice was taken while maintaining a CO distance of 1.1 Å and scanning the $\nu_{Cl\text{-}CO}$ stretch and $\theta_{Cl\text{-}CO}$ bend. Note the angle only goes up to 180 degrees for the anion. 48

Figure 28 - A ‘slice’ of the 2D potential energy scan of the Br-CO anion (top) & neutral (bottom) species at MP2/aug-cc-pvdz. This slice was taken while maintaining a CO distance of 1.2 Å and scanning the $\nu_{Br\text{-}CO}$ stretch and $\theta_{Br\text{-}CO}$ bend. 49

Figure 29 – A ‘slice’ of the 2D Potential energy surfaces of the $Cl^{-}\cdots CO$ anion (top) and neutral (bottom) species using the DFT basis set MO62X/aug-cc-pVDZ. The CO distance was frozen at 1.1 Å while scanning the $\nu_{Cl\text{-}CO}$ stretch and $\theta_{Cl\text{-}CO}$ bend. Note the angle only reaches 180 degrees. 51

Figure 30 – Predicted spectra overlayed on the experimental spectrum obtained of $Cl^{-}\cdots CO$. Both basis sets (top: pVDZ, bottom: pVTZ) predict the $0 \leftarrow 0$ as the most probable transition. The bright green corresponds to hot band transitions from the v=1 vibrational level. 54

Figure 31 - Predicted spectra overlayed on the experimental spectrum obtained of $Br^{-}\cdots CO$. Both basis sets (top: pVDZ, bottom: pVTZ) predict the $0 \leftarrow 0$ as the most probable transition. The bright blue corresponds to hot band transitions from the v=1 vibrational level. 56

Figure 32 – Schematic showing how selected ions would be deflected using 99 % transmittant grids (region 2) with switched voltages and then have electrons photodetached (region 4). Taken from reference.[22] 58

Figure 33 – Predicted spectra overlayed on the experimental spectrum obtained of $Cl^{\cdots}CO$. Both basis sets (top: pVDZ, bottom: pVTZ) predict the $0 \leftarrow 0$ as the most probable transition. The bright green corresponds to hot band transitions from the v=1 vibrational level. 65

List of Tables

Table 1 – Typical TOF-PES experimental conditions. 19

Table 2 – Calculated data for the minimum energy structures of the clusters $Cl^{-\cdots}CO$ and $Br^{-\cdots}CO$ and their constituents at MP2/aug-cc-pVDZ and MP2/aug-cc-pVTZ. Provided are the internal coordinates (r in Å and θ in degrees), harmonic vibrational frequencies (ω in cm^{-1}, symmetries included, intensities in km mol^{-1} in bold font style), zpe (in kcal mol^{-1}), MP2 energies (E_{MP2} in hartrees) and BSSE and zpe corrected energies (also in hartrees). Values in parentheses are differences to literature.[23] 39

List of Abbreviations

TOF-PES: Time-of-flight Photoelectron Spectrometer

TOF: Time-of-flight

PES: Photoelectron spectroscopy

1. Introduction

Photoelectron spectroscopy (PES) is a valuable technique permitting the examination of the world at a molecular level, by analysing energy levels within atoms and molecules. Ultraviolet photoelectron spectroscopy uses UV radiation to provide information about the valence energy levels in the molecule and how chemical bonding is achieved. This is fundamental information revealing how chemical reactions occur. Dissociation energies can be easily determined with PES for anion-neutral complexes.

In the gas phase clusters can form, and again PES can be utilised to monitor the process of each addition to the solvation shell. By understanding processes at a molecular level we can begin to perceive how solvation in condensed states occurs.

1.1. Project aims

This project aims to record experimental photoelectron spectra of the $X\cdots(CO)_n$ (X = Cl, Br) clusters and to compare them with *ab initio* calculations that will predict cluster structures, energetics, and formulate potential energy surfaces thereby creating a predicted photoelectron spectrum. The results will hopefully provide information about the characteristics of the energy levels of the neutral species. Experimentally, the PES technique also allows the monitoring of 'microsolvation' processes; through recording spectra of larger clusters where an additional CO monomer is added to the 'solvation shell' around a halide ion core.

By comparing experimental results to theoretical calculations improvements to theoretical basis sets and methods can be made for future computations. Additionally, the potential energy surfaces formulated for the neutral and anion species will allow us to discover more about how carbon monoxide interacts with halogens. Such an understanding will have relevance to reactions occurring in our atmosphere and other planetary atmospheres.

1.2. Intermolecular interactions

Chemistry is defined by reactions, which are the interactions between reactants to form products, and the reaction pathway(s) they follow. To understand the reaction taking place, and be able to predict the products formed, or the path the reactants will follow, the way in which the reactants interact is vital knowledge. Once this knowledge is acquired then the power to control reactions becomes available.

When two reactants collide, they not only require the correct geometry, but sufficient energy to form products. Nevertheless these 'products' may only be intermediate states; therefore not the most stable conformation or configuration of the product. These intermediate states are usually quite unstable but their geometries can be useful in studying how reactions take place.

1.3. Potential energy surfaces

A graphical description of a reaction process can be depicted by a potential energy surface. The potential energy is a function of different important geometric factors such as the intermolecular distance of the reactants, bond angles and bond lengths of constituents of the cluster. In Figure 1 the most stable (i.e. energetically favourable) state is the one at the global minimum.

Local minima are intermediate states and any maxima on the surface represent transition states. For each conformation there are numerous discrete vibrational states (due to nuclei vibrating) and rotational states (due to the molecules rotating), that the cluster can occupy.

In anion photoelectron spectroscopy an electron is ejected from an anion species to form the neutral. The process is in reality a transition from the anion's potential energy surface (usually lower as it is more stable) to the (higher) neutral surface.

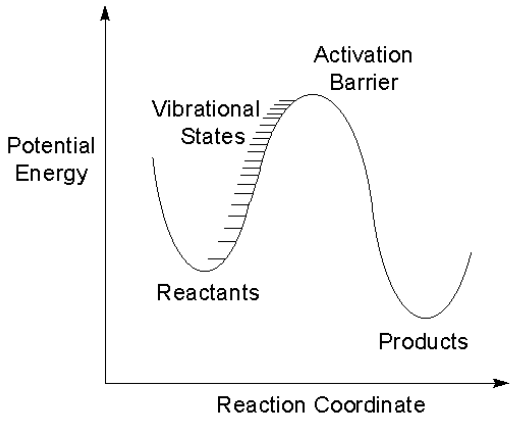

Figure 1 - A typical potential energy surface.[1]

1.4. Atmospheric chemistry

The Earth's atmosphere is only a thin layer (less than 2% of the Earth's radius) of gases protecting us from harmful rays such as ultraviolet radiation from the sun. More than 99% of the mass of our atmosphere lies below 30 km from the Earth's surface, and it contains mostly N_2 (78.08 %), O_2 (20.95 %), Ar (0.93 %) and CO_2 (0.03 %).[2]

The atmosphere is commonly divided into layers based on temperature variations (see Figure 2). The two lowest layers are the troposphere (0 - 17 km) and the stratosphere (the next 30 - 40 km) which are divided by the tropopause (a hypothetical boundary) that varies in altitude depending on the season and latitude. The ozone layer is contained within the stratosphere at about 25 – 30 km and is about 20 km thick. Beyond the stratosphere lie the mesosphere, thermosphere and exosphere.

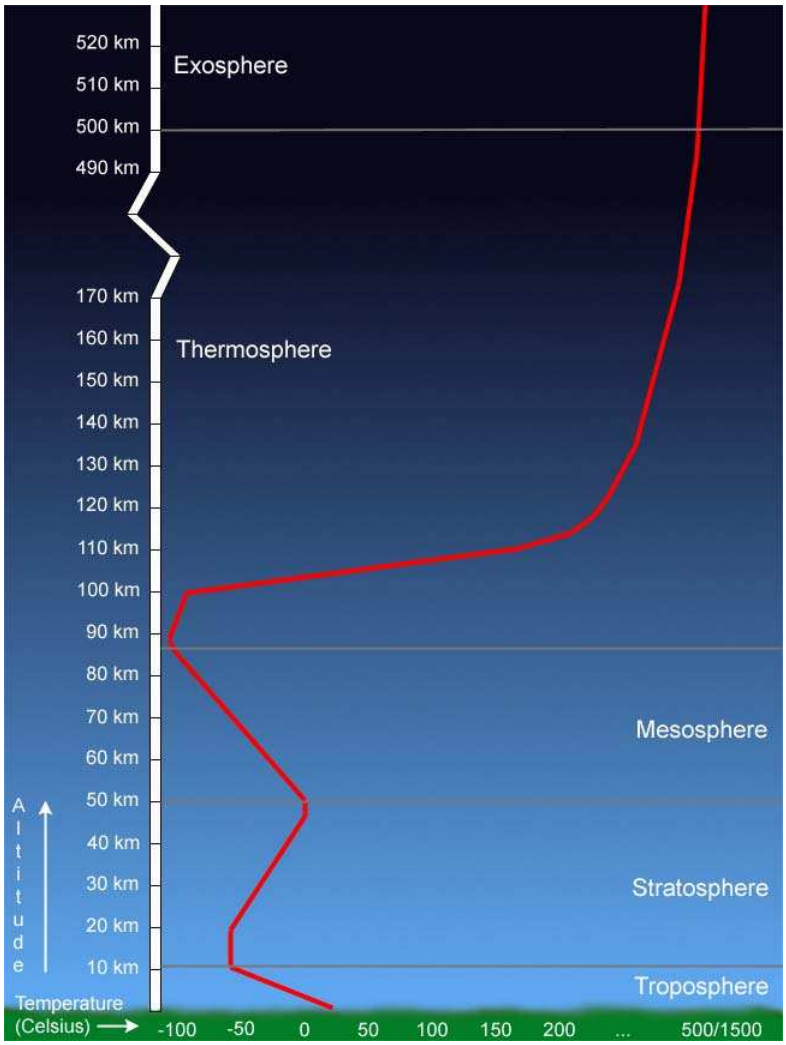

Figure 2 - The temperature-altitude profile for the Earth's atmosphere on which the boundaries between the five different atmospheric layers are based on.[3]

1.4.1. Ozone

Ozone (O_3) plays an extremely important role in protecting life on Earth as it absorbs virtually all ultraviolet radiation between wavelengths of ~240 – 290 nm coming from the sun.[2] It is effectively the sole filter preventing this radiation from reaching the Earth's surface, which is fatal to simple unicellular organisms and damaging to larger plants and animals. Ozone is only found in trace amounts throughout the atmosphere and so any shift in concentrations can cause a dramatic effect on the transmission of ultraviolet radiation.

It has been found that through catalytic processes, odd oxygen (O_3 and O) are lost via the pair of reactions (equations (1) and (2)) where X can be a number of species including chlorine, bromine and the hydroxyl radical (OH).[2]

$$X + O_3 \rightarrow XO + O_2 \quad (1)$$

$$\underline{XO + O \rightarrow X + O_2} \quad (2)$$

$$O + O_3 \rightarrow O_2 + O_2 \quad \text{(net)}$$

This means that while ozone is lost, the species causing the reaction is still available for further catalysis. It is for this reason that restrictions have been placed on chlorofluorocarbons (CFCs) entering our atmosphere.

1.4.2. Carbon monoxide

Carbon monoxide is only a trace element in the Earth's atmosphere (0.04 - 0.2 ppm by volume) as well as in Jupiter's atmosphere (0.002 ppm), but is much more abundant on Neptune (1.2 ppm), Venus (30 ppm), Titan (a moon of Saturn; 60 ppm) and Mars (700 ppm).[2] Despite only being present in trace amounts, carbon monoxide nonetheless plays an important part in the chemistry of our atmosphere, albeit in an indirect manner.

In the troposphere a major natural source of carbon monoxide comes from the oxidation of methane,

$$CH_4 + O_2 \xrightarrow{\text{OH, light}} H_2O + CO + H_2 \quad (3)$$

Non-methane organic compounds contribute up to 50% of CO emissions, while plants and micro-organisms emit smaller amounts. The majority (60%) of CO comes from natural sources such as bushfires and volcanic eruptions.[2]

Loss of carbon monoxide occurs mainly through oxidation to form carbon dioxide (equation (4)), which greatly decreases the concentration of OH (~ 70%), having a strong, indirect impact on stratospheric ozone.[2]

$$OH + CO \rightarrow H + CO_2 \quad (4)$$

The remaining 30% of OH would react with methane, of which CO is a product (see equation (3)), which again leads to a loss of OH via equation (4). Carbon monoxide has a residence time of about two months in our atmosphere, considered a moderate lifetime, and can travel distances of up to 100 km.[2]

1.4.3. Halogens

The halogens are well-known to cause havoc in our atmosphere's chemistry, especially in the ozone layer, and are found in a variety of compounds. A few of them (methyl halides and inorganic chlorine and bromine) come from natural origins such as from the ocean and volcanic eruptions, as well as salt flats and inland bodies of salt water.[2] The majority of halogens however derive from man-made sources, such as chlorofluorocarbons (CFCs).

Free halogen atoms react in a number of processes in both the stratosphere and troposphere, the most important being: "(1) direct attack on organic substrates to initiate oxidation chains; (2) formation of organo-halogen compounds; and (3) involvement in catalytic cycles that would destroy tropospheric ozone".[2] Bromine has proved to be an even more effective catalyst than chlorine in catalytic ozone destruction.[2]

The chlorine atom has been shown to react with carbon monoxide (see equation (5)) to form the unstable complex ClCO ($k_{-5} >> k_5$) although the stability has been shown to depend on the buffering gas (M the third body).[4]

$$Cl + CO + M \xrightarrow{k_5} ClCO + M \quad (5)$$

$$Cl + CO + M \xleftarrow{k_{-5}} ClCO + M \quad (6)$$

The rate constant for reaction (5), determined experimentally in air, is approximately eight times smaller than that for the reaction of CO with OH (equation (4)). As a result, the "dominant sink" for CO is the reaction with the OH radical in the troposphere, however when the concentration of Cl is greater than or equal to OH, such as in polar regions at the marine boundary layer during sunrise "the Cl + CO reaction will be a significant sink".[5]

This means that the reaction between chlorine and carbon monoxide can decrease the amount of ozone reacting with chlorine, but it also decreases the available carbon monoxide to react with the hydroxide radical. This would therefore leave more of the hydroxide radical to react with ozone.

One estimate of the efficiency of bromine atoms at catalysing ozone decomposition is 58 times faster than chlorine.[2] Bromine would catalyse ozone's decomposition in a pair of reactions similar to that of chlorine (equations (1) and (2)). The question remains then why bromine is more effective than chlorine at catalysing ozone. Although there may be more bromine available to react with ozone than chlorine, it can also react in such a manner that requires neither atomic oxygen nor light to regenerate the halogen atom, where ClO (from equation (2)) cannot.

$$BrO + BrO \rightarrow Br + Br + O_2 \qquad (6)$$

Although there have been matrix IR studies on the BrCO radical,[6] there is no photoelectron experimental information reported, only theoretical geometries[7] have been calculated (detailed in the Results section p38).

1.4.4. Extraterrestrial systems

It would be interesting to discover the importance of carbon monoxide and halogen interactions in different atmospheres to our own. So far only the atmosphere of Venus has been shown to contain both chlorine and carbon monoxide.

Venus is the nearest planet to the sun and has an atmosphere which is "about a hundred times as massive as that of the Earth".[2] Venus is exposed to nearly twice the amount of energy from the sun (~2600 W m^{-2}) compared to Earth. HCl (and HF) have been identified in the Venusian atmosphere by Earth-based infrared spectrometry, but unfortunately only due to an unbroken layer of cloud that lies about 70 km from the surface only concentrations at higher altitudes can be examined.

Atomic chlorine and carbon monoxide on Venus are thought to react as per equation (5), and feature heavily in cycles forming CO_2 (the main constituent of the Venusian atmosphere at 96.5 %) from CO and O.

1.5. Cluster science

Clusters, i.e. two or more species interacting with each other, have been widely studied.[8] Interest started in the mid-nineteenth century with colloids, aerosols and nucleation phenomena and was renewed during the First World War when producing smokes and fogs. Clusters were observed several decades ago using mass spectrometers and then once lasers were implemented in the 1970s, could be investigated in more detail.

There are clusters of the type A_n^-, where there is an additional electron that is delocalised over the whole cluster; however those clusters which have a charged core that is 'solvated' by neutral species in the form of $X^{\pm}(M)_n$ are the focus for this project.

Clusters formed can have small, weakly bound (van der Waals) forces between molecules such as those under investigation here, or experience stronger intermolecular forces. It has been found that the intermolecular forces are not additive,[9] i.e. the interactions between molecules is not the sum of all the interactions at play.

The spectroscopic study of clusters is still a new field of research, and there is much more knowledge required before we can begin predicting whether clusters can be characterised as liquids or solids. Clusters in the gas phase also experience solvation similar to how solvation occurs for solution-based reactions. For negative ions denoted by A^- solvated by a molecule B and M a third body, the solvation proceeds as in Equation (7).

$$A^-(B)_n + B \xleftrightarrow{M} A(B)_{n+1} \tag{7}$$

By investigating solvation of the clusters in the gas phase the opportunity to study them at the microscopic level becomes accessible. The term 'microsolvation' is used to highlight the 'bare' ions in the gas-phase with few solvating ligands in comparison to solutions

where the ions are in bulk. Such small 'sections' of the condensed phase allow a simplified picture of the overall situation, and can also simplify chemical reaction dynamics.

PES is a technique that permits each individual addition to the cluster solvation shell to be resolved. By understanding solvation at a molecular level, it is hoped that solvation can be better understood in solutions and bulk materials. Anion PES in the gas-phase looks at the solute-solvent (and solvent-solvent) interactions of anion cores with neutral ligands. There is a great advantage to combining a mass spectrometer to the photoelectron spectrometer as solvation processes can be followed without obstacles as clusters increase in size.

1.6. Photoelectron spectroscopy

Photoelectron spectroscopy, a technique based on the photoelectric effect, is used to study energy levels in atoms and molecules and can be used with solids, liquids and gases. Anion PES provides information over the neutral species by photodetaching an electron from the anion species. By incorporating it in the gas-phase it is especially useful for studying bond dissociation energies.[10]

1.6.1. The Photoelectric effect

The photoelectric effect can be described by an incoming photon which will interact with an atom or molecule. If the photon has sufficient energy to ionise the species (i.e. exceeds the binding energy), an electron is ejected with kinetic energy equal to the difference in energy between that of the incoming photon and the electron binding energy:

$$e^-_{KE} = h\nu - e^-_{BE} \qquad (8)$$

The ejected electrons (photoelectrons) have kinetic energies that are characteristic of the energy levels of the atom or molecule being investigated. X-rays and ultraviolet radiation

are used in PES to provide the necessary energy to eject an electron from the core and valence levels respectively.

In Figure 3 only the green and blue wavelengths have sufficient energy to overcome the work function (electron binding energy for solids) of the potassium. As the blue wavelength has a greater initial energy the resulting photoelectron has a greater velocity.

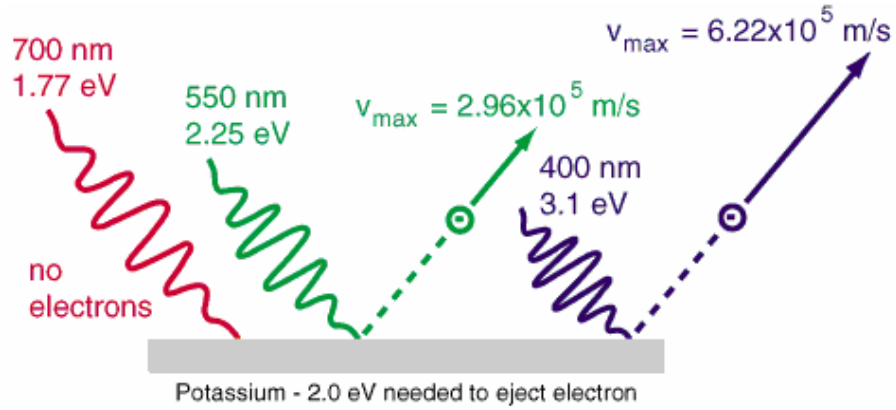

Figure 3 – The photoelectric effect on solid potassium. Only photons with permissible energies will be absorbed, causing photoelectrons to be emitted with the excess energy being converted into kinetic energy.[11]

1.6.2. Anion photoelectron spectroscopy

In anion photoelectron spectroscopy a neutral species is investigated by ejecting a photoelectron from the corresponding anion species. The difference in energy between the anion and neutral's ground electronic states (at the lowest vibrational-rotational level) is referred to as the adiabatic electron affinity, EA_a (see Figure 4), which can be measured very accurately.[10]

Another value commonly referred to is the dissociation energy of a molecule or cluster (D_0) which is the depth of the potential well (D_e) with the zero point energy (the energy difference between the bottom of the potential well and the ground state at the lowest vibrational-rotational level) removed, to take into account the vibrations of the bond.

This honours project will use the newly built photoelectron spectrometer coupled to a time-of-flight mass spectrometer to record photoelectron spectra of the chlorine and bromine carbon monoxide van der Waals clusters. This will be done by photodetaching their anion counterparts.

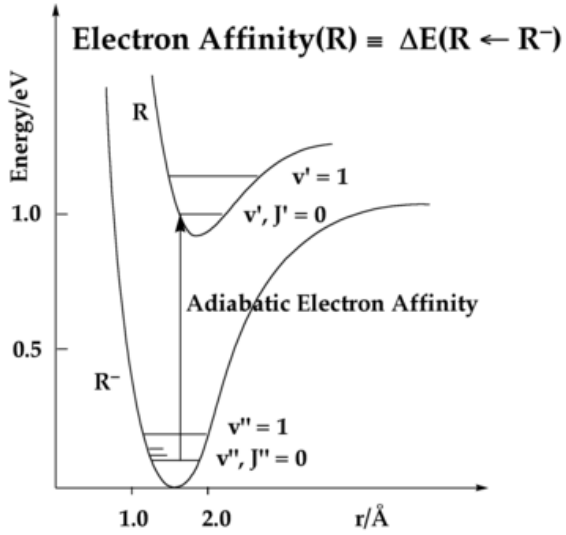

Figure 4 - The adiabatic electron affinity shown on an anion to neutral progression.[12]

2. Method & materials

2.1. TOF-PES

The Time of Flight mass spectrometer coupled with a PhotoElectron Spectrometer (TOF-PES) is a home built apparatus capable of recording photoelectron spectra of mass selected anion-molecule clusters. The time-of-flight mass spectrometer is based on the design of Wiley and McLaren.[13], while the photoelectron spectrometer is of the magnetic bottle design pioneered by Smalley *et al.*[14] The construction and preliminary testing of the TOF-PES at UWA has been described previously in detail by LaMacchia,[15] while further modifications are discussed by Quak.[16] A simplified schematic of the equipment is shown in Figure 5.

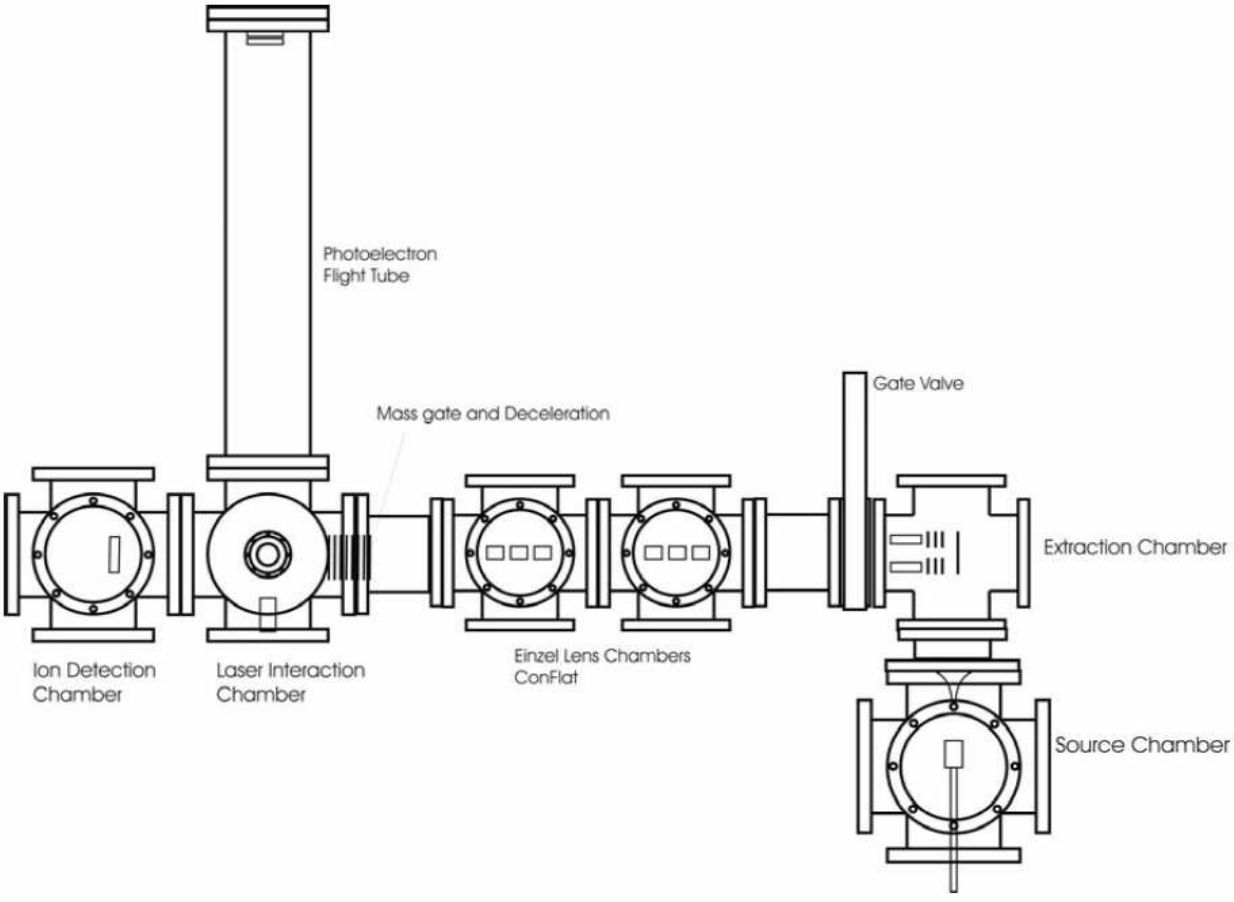

Figure 5 - The time-of-flight mass spectrometer coupled to the photoelectron spectrometer in the Wild laboratory.[17]

The TOF-PES apparatus consists of an ion source, TOF extraction plates, electrostatic lenses, ion and photoelectron detectors and a fixed frequency Nd:YAG laser (Neodynium:Yttrium Aluminium Garnate $Y_3Al_5O_{12}$). To achieve high vacuum, and to allow regular maintenance of the ion source, the apparatus is divided into two parts by a gate valve. The pressure during experiments (with the valve open) in the laser interaction chamber is typically ~1 x 10^{-7} Torr, while in the source chamber it is ~1 x 10^{-5} Torr. When no experiments are being conducted (hence with the gate valve closed) the ion source side is maintained at ~1 x 10^{-8} Torr and the detector side at ~2 x 10^{-9} Torr.

The vacuum is achieved by two types of pumps, diffusion and turbomolecular, which are backed by rotary pumps. The diffusion pumps use polyphenol oil (Santovac 5) oil and are backed by the Edwards Model E2M40 rotary pump while the KYKY (600 Hz) and Edwards (1000 Hz) turbomolecular pumps are backed by two Edwards Model E2M5 rotary pumps.

The $Cl^{-}\cdots CO$ and $Br^{-}\cdots CO$ clusters were produced in an electron beam-crossed expansion using trace amounts of vapour of carbon tetrachloride (CCl_4) as the Cl^- ion precursor and dibromomethane (CH_2Br_2) for the Br^- ion precursor mixed with carbon monoxide (CO) and argon gas in a 15:80 ratio.

Photodetachment is achieved by using the fourth harmonic (266 nm) of the Nd:YAG laser pulsed at 10 Hz. The setup has been recently modified to include a half-wave plate and beam splitter for intensity attenuation and a telescope arrangement to reduce the beam diameter (see Figure 6). Knife edges have also been incorporated onto the light baffles (see Figure 11).

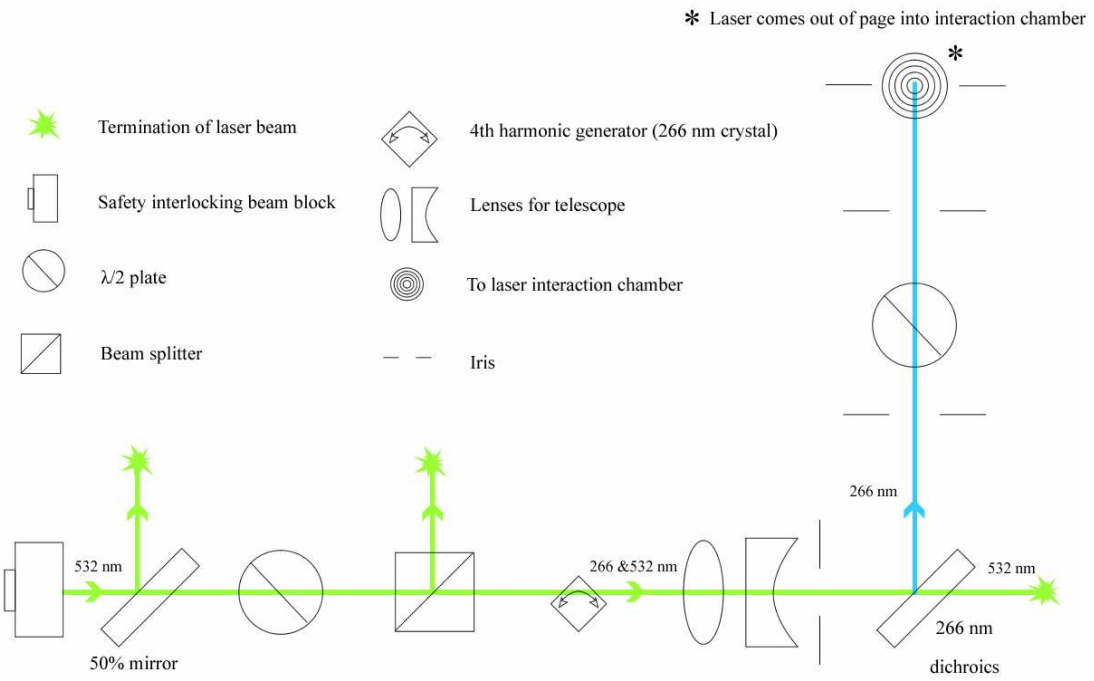

Figure 6 – Schematic of the current laser setup.

2.2. Experimental method

Both LaMacchia[15] and Quak[16] have explained in detail the procedure used to create the anion-molecule complexes from a gas mixture however the following is a description of the conditions employed for the present study. For those readers interested in a further discussion of the configuration of each particular section of the TOF-PES and its function please refer to their works.

2.2.1. Gas mixture for halide-carbon monoxide clusters

The gas mixture containing carbon monoxide, a source of halide ions and argon, the buffering gas, is composed in the gas mixing station. Argon is used as a buffer gas because it has been shown to improve resolution of spectra by vibrational cooling.[18] Through collisions of the clusters with argon effects from 'hot bands' (when populations are spread in vibrational states other than the ground state) are reduced. This gas mixture is then pulsed to the source chamber through the gas nozzle and crossed with energetic electrons.

A preliminary study was undertaken to determine the best ratios of gas mixture constituents to produce clusters of the greatest intensity. This was not comprehensive however it was found that a ratio for X^-:CO:Ar of approximately 1:15:80 provided reasonable yields of the anion species. Other ratios attempted were 1:2:93, 1:5:90 and 1:10:85.

2.2.2. Making the anion clusters

The electrons that coincide with the expanding gas mixture are produced in the source chamber by passing a static current of typically 3.5 A through twin rhenium filaments and subsequently pulsing a high voltage (typically -200V) to the assembly. The resulting electrons interact with the gas expansion to form a plasma in which the charged clusters are produced via the scheme illustrated below.

$$Ar + e^-_{fast} \rightarrow Ar^+ + e^-_{slow} + e^-_{fast} \quad (9)$$

$$CCl_4 + e^-_{slow} \rightarrow [CCl_4]^{-*} \rightarrow CCl_3 + Cl^- \quad (10)$$

$$Cl^- + CO \rightarrow CO \cdots Cl^- \quad (11)$$

To reach the extraction chamber the plasma passes through a conical skimmer of either 3 mm or 1 mm and is collimated in the process. In the extraction chamber the charged clusters (anions in these experiments) are deflected into the time of flight mass spectrometer by pulsing large negative voltages to the extraction plates (see Figure 7).

The potential difference between the back and third plate (at ground potential) defines the kinetic energy of anions, while the potential difference between the back and second plate determines the position of space focussing along the time of flight axis. Space focussing is defined as the point along the TOF axis where ions of the same mass/charge ratio arrive simultaneously. The anions all enter the time of flight tube with the same kinetic energy, a vital requirement for experiments to succeed as will be explained in more detail later.

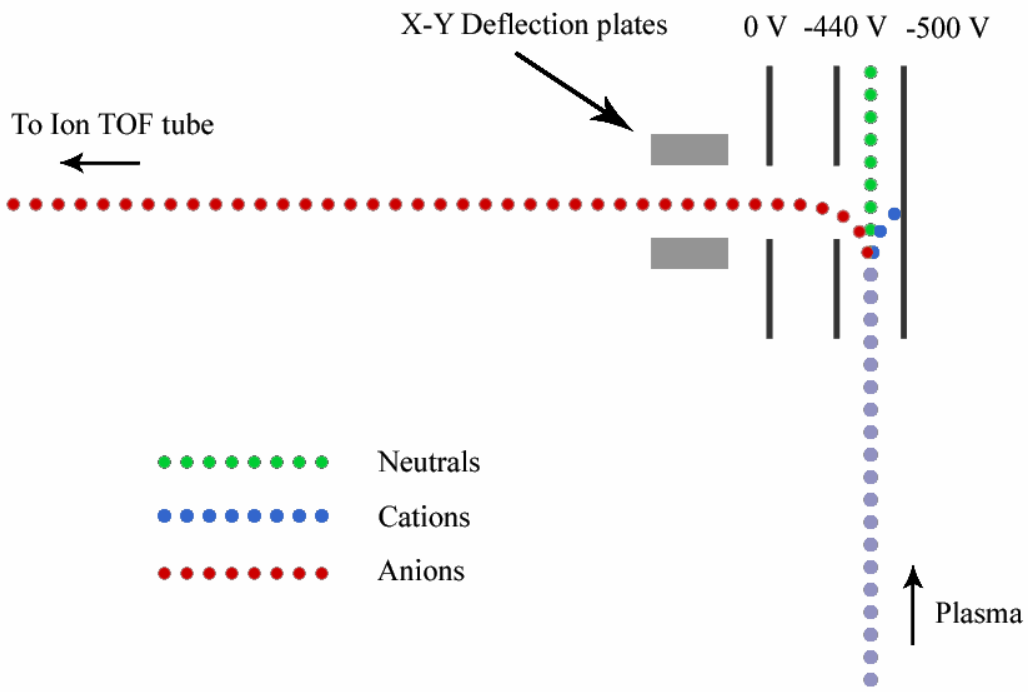

Figure 7 – Schematic demonstrating the deflection of anions towards the time-of-flight tube using negatively charged plates.

Finetuning of the anions' trajectory along the TOF axis is achieved with the X-Y deflection plates (Figure 7). It should be noted that the cations residing in the plasma originating from the ion source are accelerated in the opposite direction to the anions and strike the back extraction plate, while the neutral species are unaffected by the potentials applied and fly on towards the end wall of the chamber.

Two electrostatic (Einzel) lenses located in the time of flight tube serve to refocus the ion beam that spreads due to Coulombic repulsion, before they arrive at the ion detector or laser interaction region

2.2.3. Selecting the ion of interest, and slowing them down

After the ions have separated along the TOF axis, a mass gate with variable timing and width permits the study of only the ion of interest. This piece of the apparatus, which comprises a stainless steel cylindrical lens, is maintained at a potential that is higher than the beam energy (typically -1 kV for an anion with 500 eV of kinetic energy). By switching off the high negative voltage at the correct time the ion of interest is allowed to pass through. Once this ion has exited the mass gate, the high negative voltage is switched on again, repelling all other anions.

To diminish the effect of the anion velocity on the photoelectron energy distribution (Doppler broadening) an ion decelerator is employed. The decelerator consists of series of circular electrostatic lenses with increasingly larger negative potentials applied to decelerate the ions before they interact with the laser.

Selecting the ion of interest requires calculations determining the time of arrival at the detector. Equations (12) and (13) are combined to form equation (14) for this purpose.

$$v = \frac{d}{t} \tag{12}$$

$$KE = \frac{1}{2}mv^2 \tag{13}$$

$$t = \frac{d}{\sqrt{\frac{2KE}{m}}} \tag{14}$$

Since the distance of the time of flight tube *d*, is fixed, then only the velocity of the ion *v*, will determine the time *t*, it takes to arrive at the mass gate and ion deceleration stack. The velocity itself depends on the mass of the ion, as the kinetic energy when entering the time of flight tube is also at a set value for all ions, as mentioned earlier. Ions with smaller mass travel faster and therefore will arrive earlier at the detector than ions with a greater mass.

2.2.4. Recording photoelectron spectra

Once the desired ion has been selected a laser pulse with wavelength of 266nm (4.66 eV) is timed to intersect the ions as they pass through the laser interaction chamber. Photoelectrons are ejected from the anion species and are directed by a bottleneck magnetic field (shown as inset in Figure 8) created by the permanent electromagnet around the flight tube in combination with a pulsed electromagnet situated close to the laser interaction region. The electrons are forced to travel down the secondary time of flight tube to the photoelectron detector. The electron will have a specific kinetic energy given by Equation (8).

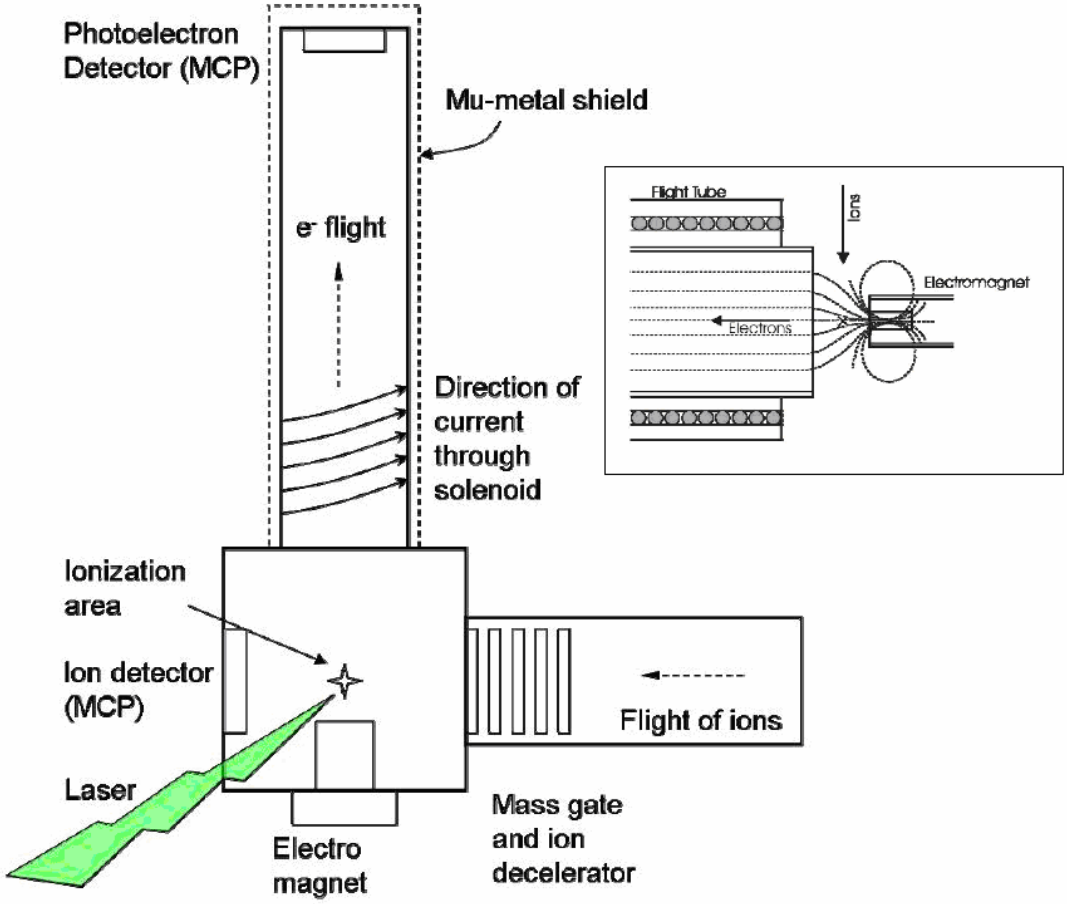

Figure 8 – Schematic showing the path of ions and photoelectrons, with an inset of a detailed view of the bottleneck magnetic field produced to trap the photoelectrons. Courtesy of Quak[16] (top) and Dr D. Wild[17] (inset, orientated 90° CCW to the main figure).

2.2.5. Operating conditions

For any given gas mixture the optimum operating conditions will be different. If, for a particular gas mixture, settings promoting favourable intensities had been found, then it was usually the case that little alteration was required after a new mixture was created. During a typical day of experimentation (e.g. Table 1) only a few adjustments would be required, provided the gas mixture had been allowed to stabilise for some small period of time first (~30 minutes). This gas mixture can remain stable for weeks.

Table 1 – Typical TOF-PES experimental conditions.

Electron filaments: 3.44 A / -247 eV
Gas nozzle: 216 V
TOF plates: -500 eV/ -443 eV
Einzel lenses: -130 V/ -44 V
X Deflection plates: 0 V/ 6 V
Y Deflection plates: 0 V/ 6 V
TOF plates timing: 855 μs

Each photoelectron spectrum was recorded over 10,000 laser shots (1000 s) and although background spectra were taken these were deemed negligible and were not subtracted from the actual spectra. A typical background spectrum can be seen in Figure 9.

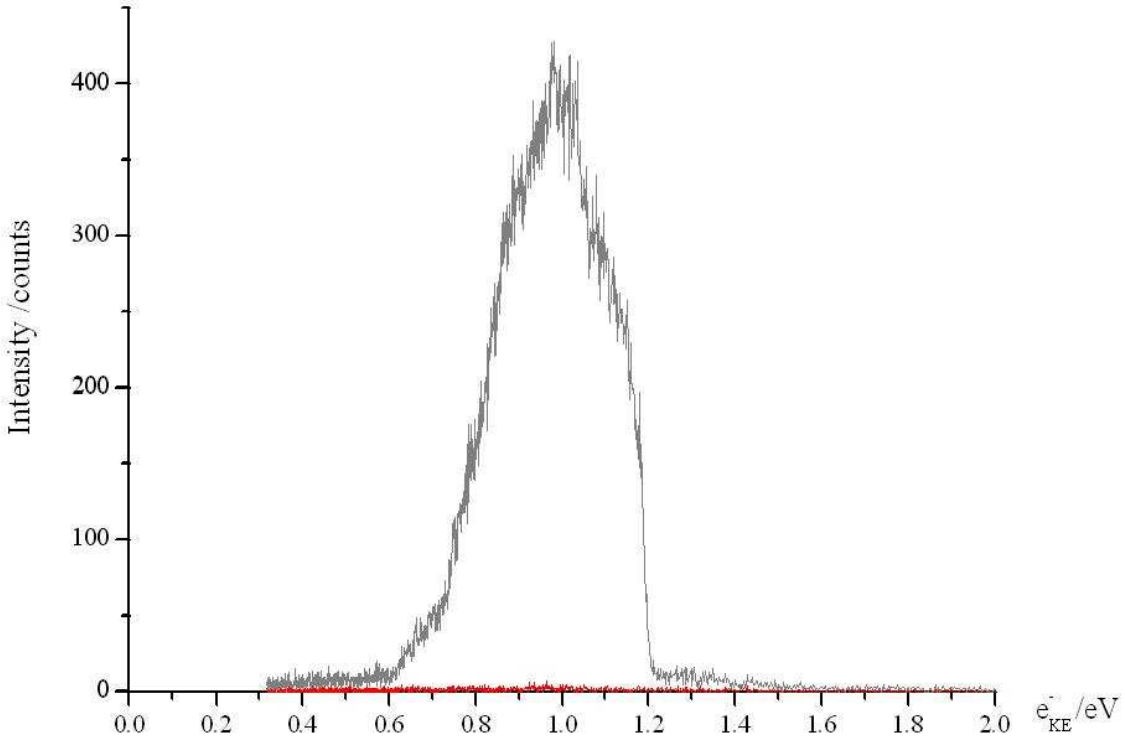

Figure 9 – Typical background (red) for a photoelectron spectrum (black).

2.2.6. Timing scheme of pulses

As the experiment is pulsed at 10 Hz, a crucial factor to optimising both the ion and photoelectron signal is the timing of the apparatus. The sequence of pulses emitted is regulated by two Stanford Research System digital delay generators (DG 535). The master delay generator controls the timing of the slave delay generator in addition to the laser pulse and electromagnet. The slave delay generator is in charge of firing the pulses at the correct timing for the rest of the equipment including the gas nozzle, electron filaments, TOF plates, mass gate and ion decelerator.

A sequence of events for a single gas pulse is illustrated in Figure 10, where t_0 is the initiating pulse of the gas nozzle. For those readers interested in a more detailed description of each event's timing please refer to Quak.[16]

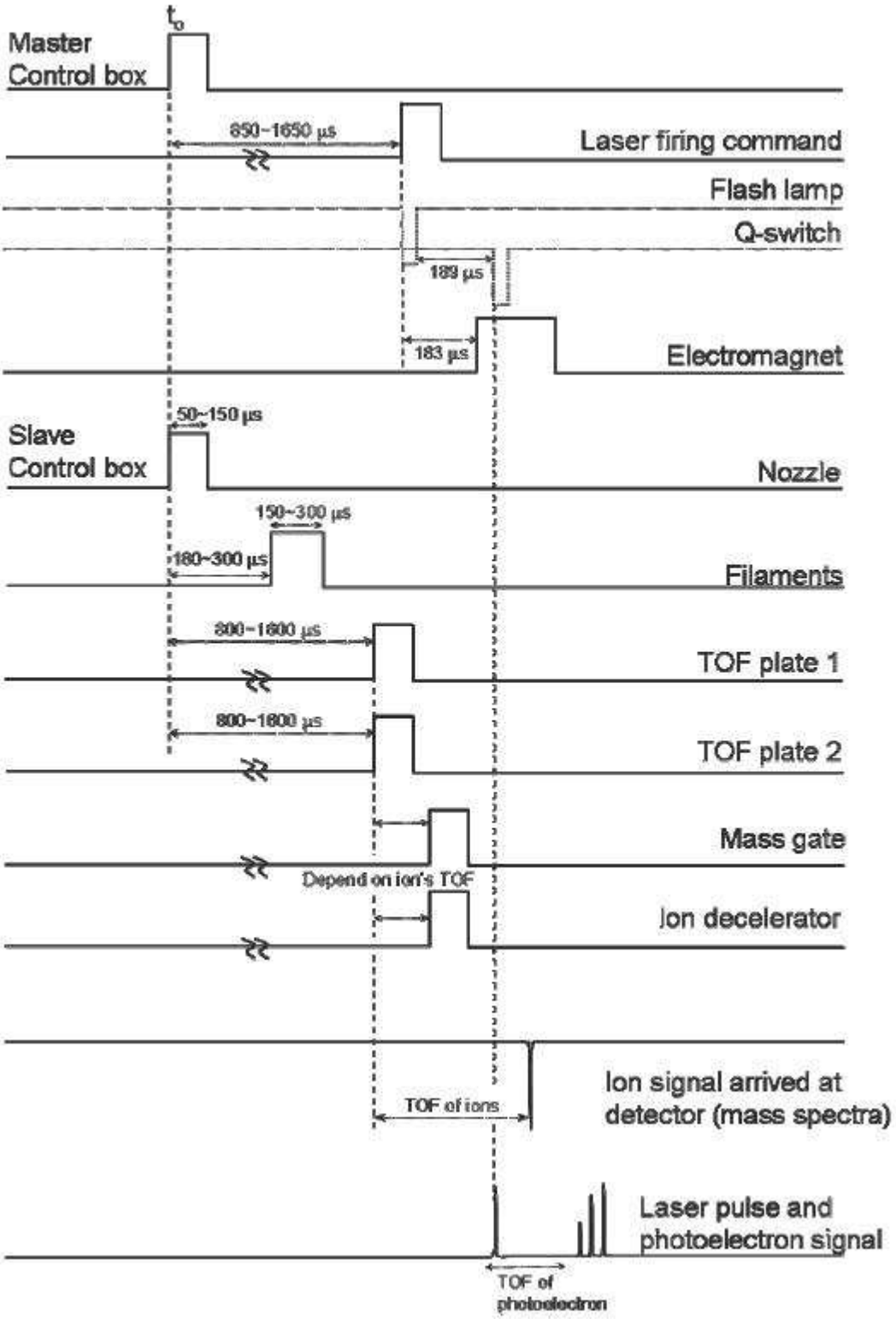

Figure 10 – Pulsing sequence for the operation of the TOF-PES. Taken from Quak.[16]

2.3. Modifications to the TOF-PES

To further improve the operational stability and the resolution of the mass and photoelectron spectrometers several modifications have been carried out on the TOF-PES since those reported by Quak.[16]

The first modification was an installation of a cryogenic trap to improve the level of vacuum in the source chamber. This trap is a small vessel incorporated into the top flange which holds liquid nitrogen thereby trapping any residual gas mixture remaining in the source chamber.

A second modification was implemented in the extraction chamber where the orifice past the X-Y deflection plates was widened and given a knife edge (Figure 11). The reason behind this modification was to reduce the number of secondary electrons that might be produced should the anions strike a metal surface during their transit into the TOF tube.

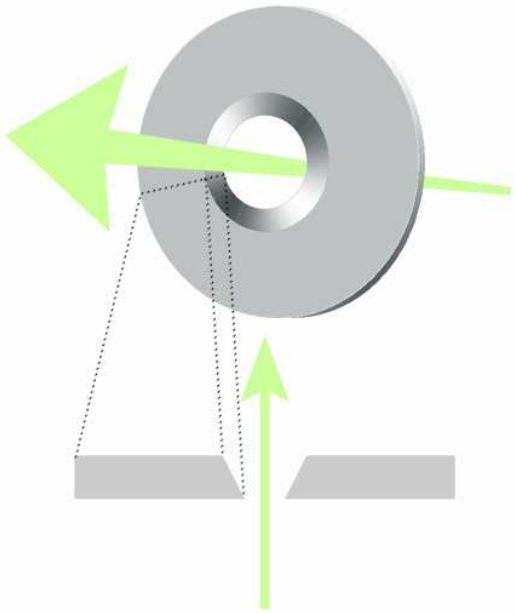

Figure 11 – Schematic of the knife-edges imposed on the orifice past the X-Y deflection plates.

Alterations were made to the electron pulse timing mechanism so that this could be regulated with more precision. This was managed by installing two new timing pieces,

thereby splitting the timing of the pulse into more appropriate sections (500 μs). By decreasing the jitter in the pulse the ion signal can be treated more precisely.

Although not a direct mechanical modification to the system, a considerable improvement in the resolution of the mass spectra and photoelectron spectra was achieved by decreasing the ion beam energy (by changing the TOF plates' voltages accordingly) from 2 kV to 500 V. This decreases the kinetic energy of the ions, so their velocity travelling through the TOF-PES will also be diminished (see Equation (13)).

By changing the potential from 2 kV to 500 V the time of flight of the ions has doubled, and so the Doppler Effect will be less pronounced as the ions velocity will not impact as greatly on the velocity of the ejected electrons, and hence the resolution of the photoelectron spectrometer improves.

Another modification designed to decelerate the ions more effectively prior to photodetachment by the laser was to change the applied potentials in the ion decelerator stack. Initially the first plate was at a high negative voltage and then decreased incrementally along the stack to ground. The deceleration in this configuration was achieved in the first few lenses of the stack, and to ensure that the ions were not re-accelerated the voltage applied to the stack was rapidly switched to ground.

From simulations it was realised that this was not optimal, and it was proven more effective to invert the stack so that the ions experience an increasingly negative potential as they proceed through the stack. The anions are then decelerated more gradually as they approach the more negative potential. The potential energy curve experienced by the ions can be described as similar to climbing a hill – they gradually lose velocity as they approach the top. With the previous setup the ions can be thought of as instantly jumping up to the top of the hill (losing kinetic energy), and then being rolled down until the slope was instantaneously flattened at some point during its descent.

During experiments it was noted that the permanent electromagnet used to create the bottleneck magnetic field to trap photoelectrons became overheated. Unfortunately water cooling was not sufficient for extended periods of time that the magnet was on during experiments. To provide more effective cooling to the electromagnet a stream of cooled nitrogen gas was passed over the magnet (in conjunction with the water cooling). The cooled stream of nitrogen was created by passing nitrogen gas from the house supply through a dewar containing liquid nitrogen. The nitrogen was supplied via a stainless steel tube to the bottom of the liquid nitrogen filled dewar, while a second tube which was situated above the level of the liquid nitrogen delivered the cooled gas to the electromagnet.

Several changes were made to the laser setup (currently configured as per Figure 6). In the first instance the orifices of light baffles inside the TOF-PES were modified with knife edges similar to the orifice in the extraction chamber, in order to reduce reflected light from reaching the laser interaction chamber as well as to reduce the beam diameter and keep it collimated (see Figure 11). Unwanted reflections can strike the inner surfaces of the chambers, producing stray photoelectrons which contribute to the background noise, so minimising these reflections is essential.

Three extra light baffles have been incorporated into the setup, which ameliorated the signal-to-noise ratio of the photoelectron spectra. A half wave ($\lambda/2$) plate cube beam splitter and polariser have also been added to aid the signal-to-noise ratio by decreasing the power of the laser beam.

It is now also possible to reduce the laser beam diameter to 6 or 3 mm (previously at 8 mm) with the ‘telescope’ lens arrangement, so a better match between the ion beam and laser beam diameters ensure optimal overlap and more efficient photodetachment. The telescope set up shown schematically in Figure 6 results in a 6 mm beam diameter and consists of a plano-convex lens (f = 40 mm) c and a plano-concave lens (f = -30 mm).

Replacing the convex lens allows control over the diameter of the laser beam, The results presented in this thesis have only been conducted with the 6 mm diameter beam.

Finally, the safety of persons conducting experiments with a laser is extremely important. Another modification to the laser system was to enclose the beam with a box purposely constructed for our particular setup, see Figure 12.

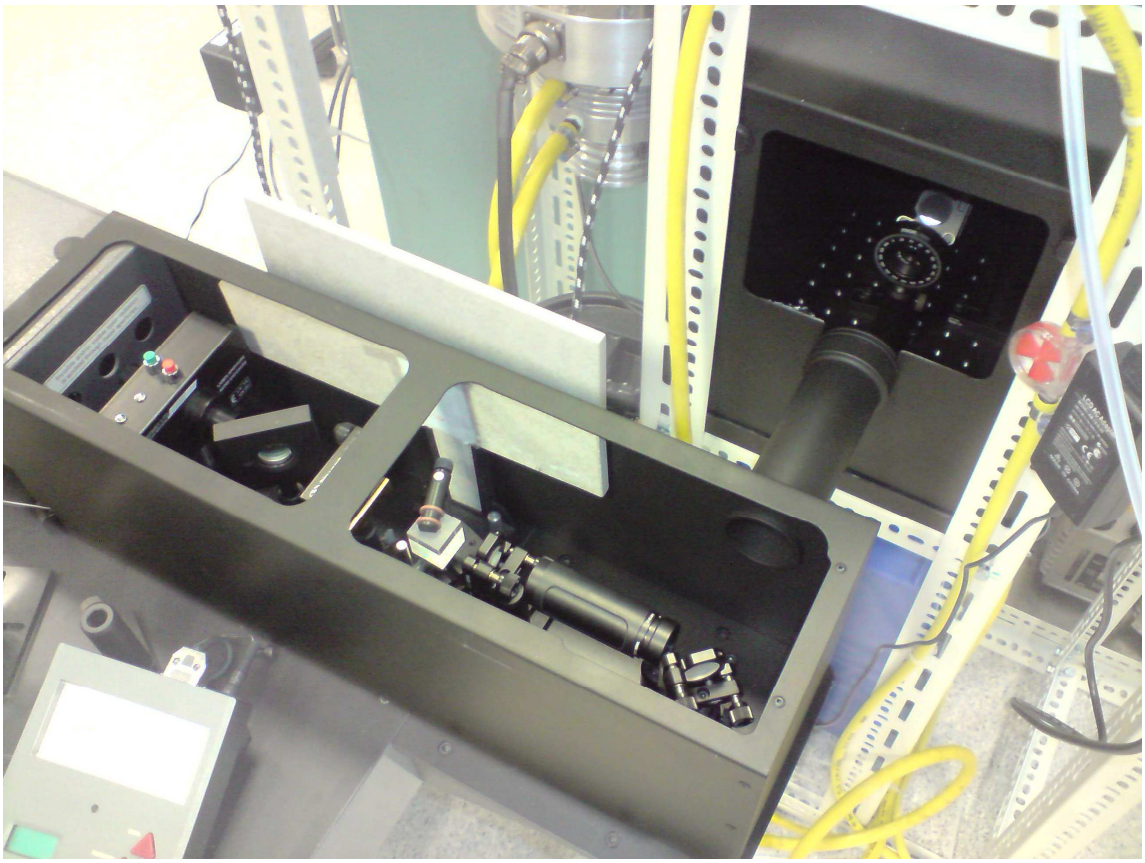

Figure 12 – Photo of the laser safety enclosure box with the lids removed.

The box consists of four sides and a lid made of two parts, coated in matte black paint, which are attached to the apparatus scaffolding where the beam is directed upwards into the laser interaction chamber. The side from which the beam enters has a cut section where the beam enters while leaving adequate room for adjustment of the optics. Another separate box covers the optics on the laser table, with a lid which can again be removed to adjust the optics. These two boxes are connected by a cylindrical tube that can easily be removed if the laser table must be shifted away from the apparatus for maintenance.

Finally, a modification (which is still ongoing) to the KYKY turbomolecular pump was required on its cooling system. Unfortunately the house water supply was not able to provide enough cooling due to blockages caused by corrosion in the water jacket of the pump. Although a temporary solution was found by thoroughly cleaning the water jacket and with vigorous pumping methods employed to clear the blockages, a more permanent remedy was necessary.

A completely new water cooling system has been devised which involves flowing distilled water housed in a 25 L vessel thereby hopefully preventing further corrosion to the water jacket. This has been installed, however due to the volume of water being recycled a means of cooling this sufficiently needed to be established. Currently a radiator with a set of three fans (such as those employed in computer systems) are adequately cooling the water being pumped around, but are still being tested for the long-term.

2.4. Theoretical methodology

The calculations required to create a predicted spectrum for both Cl···CO and Br···CO complexes have been performed on the programs Gaussian 03,[19] Gaussian 09,[20] GAMESS [21] and LEVEL 8.0.[22] The clusters are optimised using Møller Plesset 2nd order perturbation theory (MP2) with Dunning's augmented correlation consistent polarised valence double and triple zeta (ξ) basis sets (aug-cc-pVXZ (X = D, T)). So that the degeneracy of electrons with antiparallel spin in the same orbital is removed, in all calculations for the neutral species the Unrestricted Hartree Fock methodology (UHF) was used.

Bridgeman *et al.*[7] and Dixon *et al.*[23] have previously calculated structural details for the neutral species using non-local density functional calculations and MP2. In order to predict photoelectron spectra of the anions more calculations were required to be undertaken, i.e. the anion species and potential energy surfaces. For this reason the neutral calculations were repeated for consistency with the data obtained for the anion species. These calculations included the double and triple ξ basis sets used.

Harmonic vibrational frequency analyses were made on the optimised geometries to ensure that these contained no imaginary frequencies (corresponding to transition states or higher order maxima). Once the optimised geometries of the ground states of both the anion and neutral species have been determined then potential energy surfaces can be graphed by scanning the energy of the cluster during a vibrational mode.

For the clusters there are two stretching modes ν_{CO} and $\nu_{X\text{-}CO}$, and one bending mode $\theta_{X\text{-}CO}$ (illustrated in Figure 13). The energy of the clusters has been calculated at the optimal geometry at each step in a range during one of these vibrational modes (a 1D scan).

It is important to note that for the potential energy scans shown in this thesis the $r_{X\text{-}CO}$ distance measured is between the halide and the centre of the carbon monoxide (Figure 13) and not the distance to the closest atom of the carbon monoxide. The angle $\theta_{X\text{-}CO}$ is similarly changed: the chloride swings around the carbon monoxide's centre, in lieu of

rotating around either the carbon or oxygen and thereby maintaining the symmetry of the cluster.

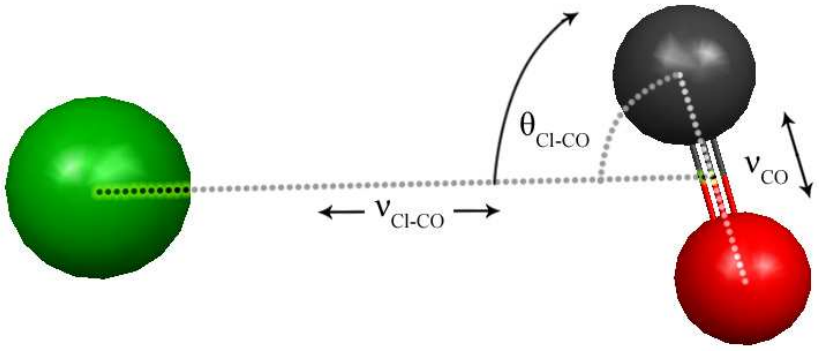

Figure 13 - The three vibrational modes possible for the three-atom system: two stretching and one bending, shown on the $Cl^{-}\cdots CO$ cluster. 1D potential energy scans involve calculating the energy at the optimised geometry in multiple steps during one such mode. Jacobi coordinates system.

The 3D scans (of which only 2D surfaces could be graphed) determined the energy of the cluster at the optimal geometry at steps during all three vibrational modes. The variables not being scanned in the mode are allowed to relax; i.e. they are not restrained to their initial values but are free to move so a more realistic energy of the cluster can be computed.

With the computations for the anion and neutral species in hand it is possible to compute the vibrational energy levels of the clusters. A Franck-Condon overlap analysis (see Figure 14) can then be made from the potential energy surfaces generated. The spectra are derived from this analysis.

The Franck-Condon overlap analysis has been computed with Level 8.0,[22] although this was only possible for the 1D potential energy surface of the $\nu_{X\text{-}CO}$ stretch (see Figure 13). This requires wavefunctions from both the neutral and anion to be compared. The most likely transition between the anion and neutral will occur where overlap is most significant

(see Figure 14). The Franck-Condon principle makes the assumption that electronic transitions are essentially instantaneous in comparison to nuclear vibrations, so that any electronic transition will occur at the same nuclear coordinates.

The Franck-Condon factors are then adjusted for the populations of each state using the vibrational partition function at 50 K, a temperature typical for clusters in a supersonic expansion.

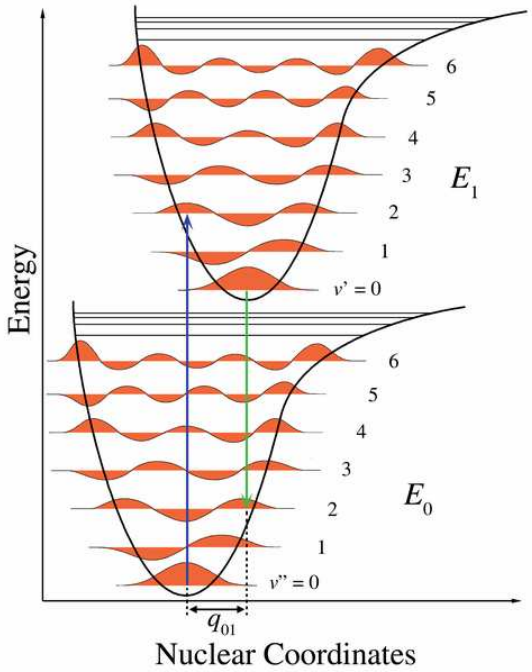

Figure 14 - The Franck-Condon principle[24] illustrating favoured electronic transitions between the vibrational states v = 0 and v = 2.

3. Experimental results & discussion

3.1. Mass spectra

The ion signal has greatly improved in stability and the intensity has remained strong during this year, as can be seen when compared to the mass spectra from LaMacchia[15] and Quak.[16] The bare ions Cl^- and Br^- reached intensities of at least 1 V, with instances of up to 2 V, and the first clusters $Cl^-\cdots CO$ and $Br^-\cdots CO$ averaged between 50 – 250 mV. The final spectrum obtained by Quak[16] had an intensity of 1.2 V for the bare Br^- and I^-. The gas mixtures were stable for multiple weeks, and only slight adjustments needed to be made to improve the intensity of selected clusters for the photoelectron spectra.

In Figure 15 the mass spectrum shows the bare ions Cl^-, Br^- and I^-, and these ions clustered with CO and Ar. In Figure 16 larger clusters are shown, as well as some exotic mixed species. It should be noted that the $Cl^-\cdots(CO)_3$ cluster is hidden under the $Br^-\cdots Ar$ peak.

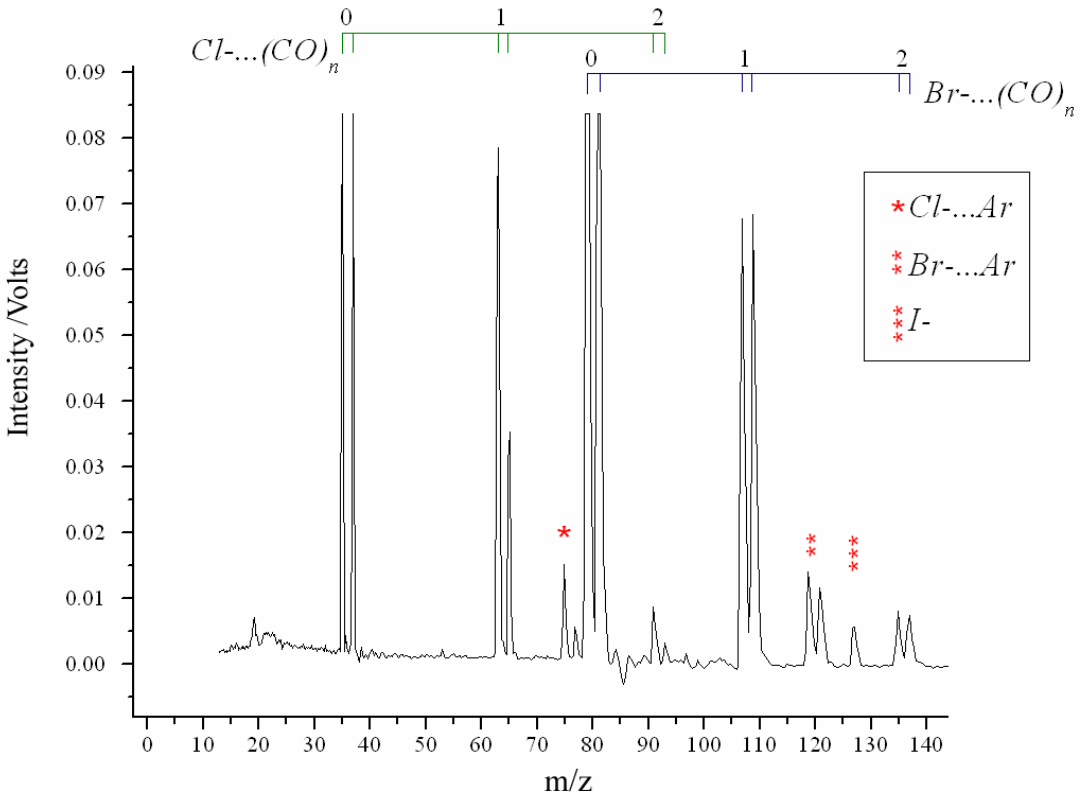

Figure 15 – A mass spectrum of bromide, chloride and their clusters with carbon monoxide. The chloride and bromide peaks are cut off (their intensities are close to 1 V) to show the weaker species.

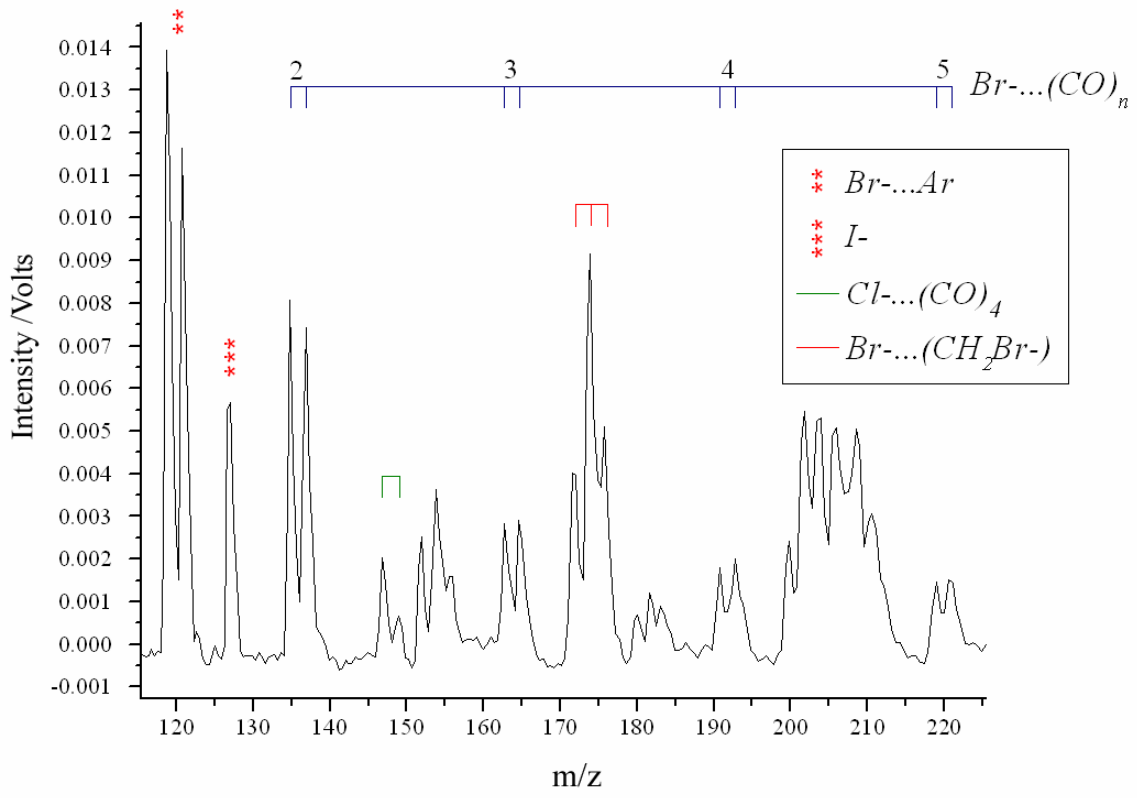

Figure 16 - Larger clusters of bromide and chloride with carbon monoxide. Other species are also shown.

The mass gate and ion decelerator were efficient at removing all ion species except the one of interest, and could even distinguish between isotopologues.

3.2. Photoelectron spectra

The photoelectron spectra taken are preliminary results, with work still to be taken further, especially to improve resolution. The full-width half-maximum (FWHM) of the peaks are on the order of ~300 meV, which leaves much to be desired. The resolution of other time-of-flight setups for anion photoelectron spectroscopy is on the order of 10 meV in the 1 eV kinetic energy range.[25] Efforts undertaken this year to reduce the FWHM are detailed on page 36.

In Figure 17 and Figure 18 the bare ion is shown alongside the cluster with CO. The two spin-orbit states $^2P_{3/2}$ (right) and $^2P_{1/2}$ (left) are visible on the Br· and Br···CO spectra but are not completely resolved in the Cl· and Cl···CO spectra. The $2P_{3/2}$ state, with the higher total angular momentum is situated to the right of the $2P_{1/2}$ state (i.e. has a lower energy) because the incomplete shell is more than half full (i.e. p^5 configuration).[26]

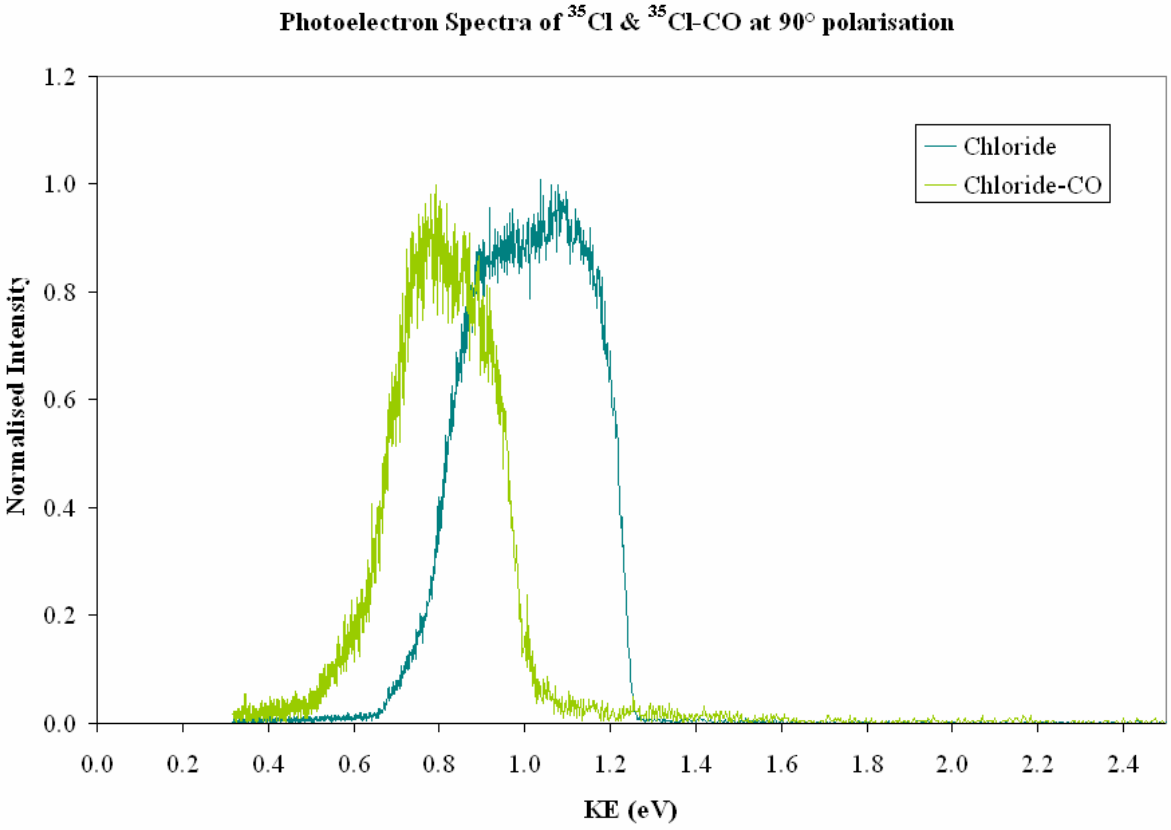

Figure 17 - The photoelectron spectra of ^{35}Cl and $^{35}Cl\cdots CO$ at 90°.

Although the absolute intensities of the spectra are insignificant (they are due to physical and experimental factors) the relative intensities of the peaks are important as they are "equal to the relative probabilities of photoionisation to different states" (also called the relative partial ionisation cross-sections).[26] Theoretically the ratios of the intensities should be proportional to the statistical weights of the neutral states produced, which is equal to 2J + 1 for atoms.[26] So for the $2P_{3/2}$ state this is: 2(3/2) + 1 = 4, and for $2P_{1/2}$ this is: 2(1/2) + 1 = 2 and gives the ratio 2:1. However the experimental results here do not reflect this ratio, which could be a sign of poor detection of the low-energy electrons.

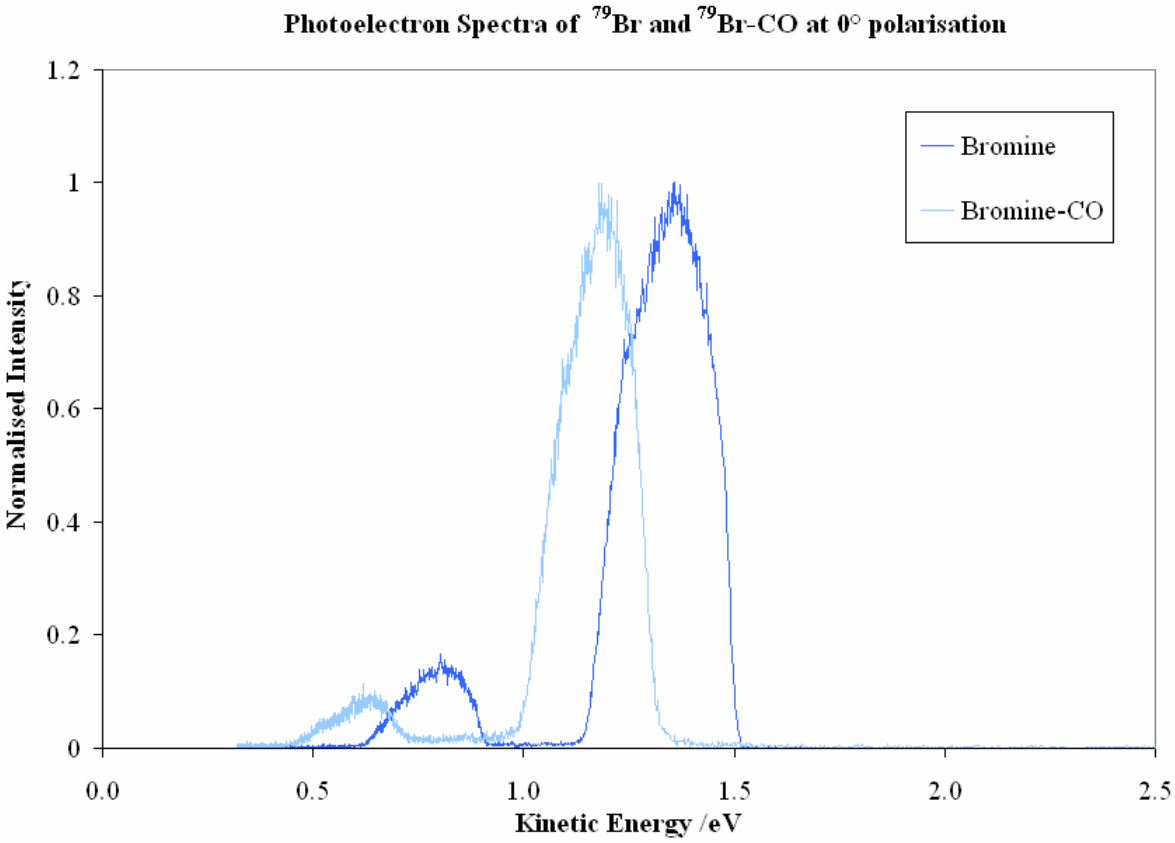

Figure 18 - The photoelectron spectra of ^{79}Br and $^{79}Br\cdots CO$.

The difference in polarisation on the photoelectron spectra can also be noted – 0° is where the laser polarisation direction is parallel to the flight axis of the photoelectrons, and 90° is where the laser polarisation direction is perpendicular. The results here reflect a more symmetrical distribution when the laser polarisation direction is parallel to the flight axis

of the photoelectrons, as this is when the velocity of the ions is not added to the spread of the photoelectrons (Doppler effect).

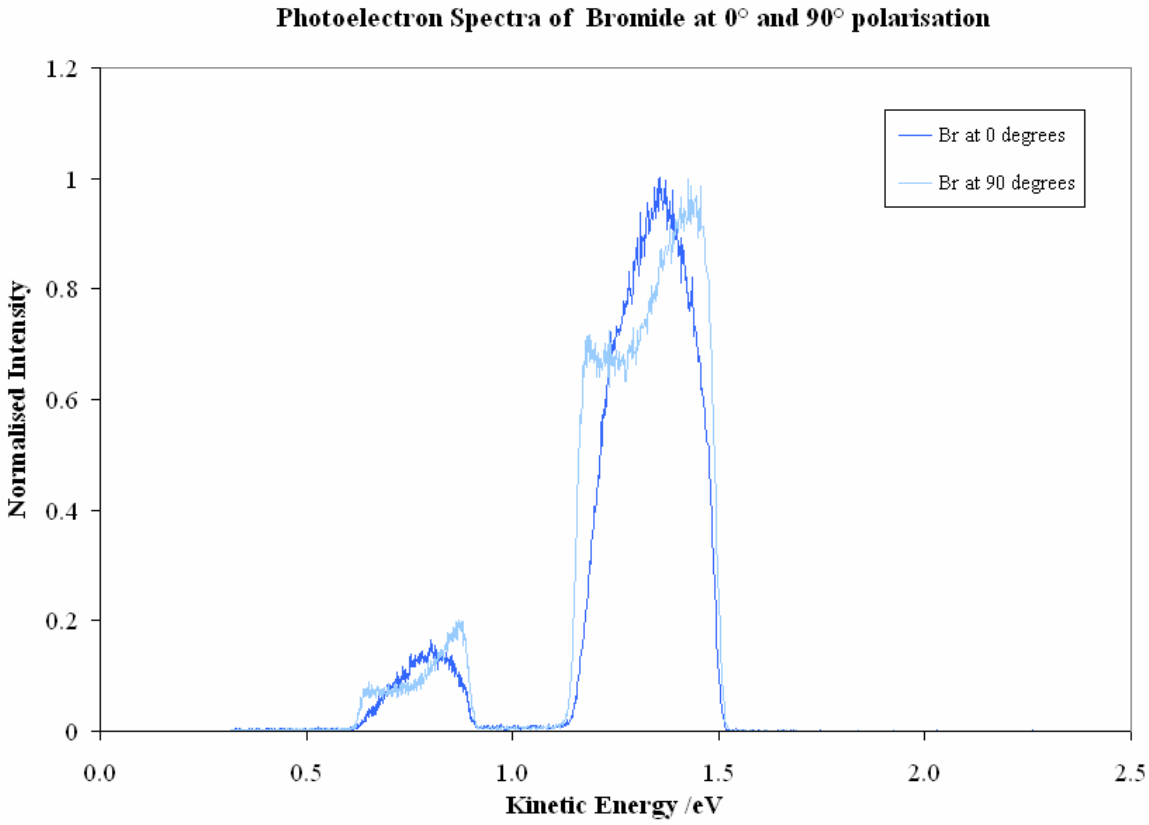

Figure 19 – A more symmetrical distribution of photoelectrons is produced when the laser polarisation angle is parallel to the flight axis of the photoelectrons (i.e. at 0°).

3.3. Improving the resolution

The effects of the ion decelerator in slowing down the ions (to decrease the Doppler broadening experienced by the photoelectrons) can be seen in Figure 20. This already shows an impressionable thinning of the spectra, but is still far from the desired resolution. The ion decelerator, when used, typically added 0.5 - 1 μs to the flight time of the anions, over a distance of approximately 40 cm (from the ion decelerator to the ion detector). There had been instances when the ion decelerator could be used to slow the ions over an even greater period of time (> 1 μs) at the sacrifice of a decrease in intensity of the photoelectron signal (on the oscilloscope) and the ion signal completely disappearing. This was due to high voltages in the ion decelerator deflecting the ions.

A new setup is also being considered for in the future that should encourage a better resolution, and is detailed in the Future Work section (page 57).

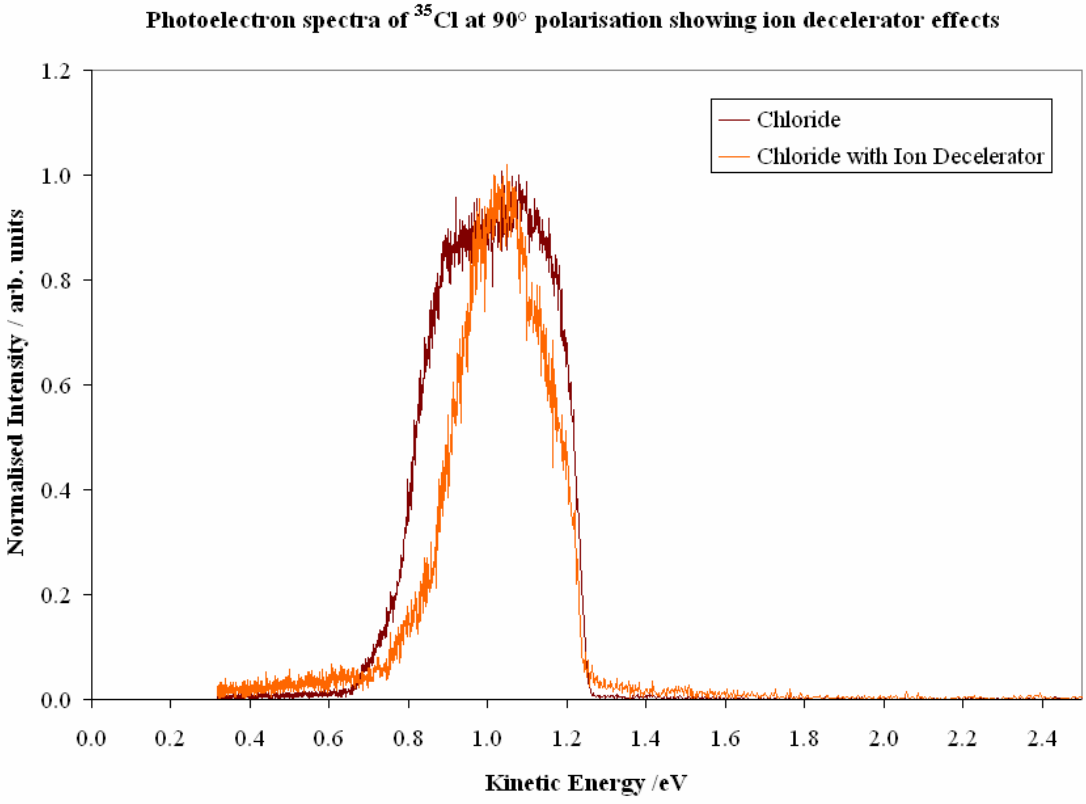

Figure 20 – Using the ion decelerator to improve the resolution of photoelectron spectra

4. Theoretical results & discussion

The calculations herein have formed the potential energy surfaces and predicted spectra using the $^2\Sigma^+$ electronic state (a linear configuration). Unfortunately it was only discovered extremely late into the project that the $^2A'$ electronic state (strongly bent configuration for Cl···CO yet linear for Br…CO)[7] was actually lower in energy (-572.8031205 Hartree compared to -572.792535 Hartree for $^2\Sigma^+$) and thus also requires investigating. It is still being determined as to why the optimised geometries of the neutral species were not calculated to lie on the $^2A'$ surface.

Contrary to Bridgeman *et al.*'s[7] results for the $^2\Sigma^+$ state of both Cl···CO and Br···CO there were no imaginary frequencies found and so the surfaces investigated did not reflect a transition state. The results presented here are therefore still viable, however further work on producing predicted spectra from the other electronic state will be needed. It is possible that the irregularities of the potential energy surface in Figure 25 are occurring because the lowest energy was calculated on a lower surface ('jumping' between surfaces).

The chloroformyl radical ClCO was observed in 1965 by Jacox and Milligan.[27] The most recent experimental work was reported in 1992 using infrared absorption by matrix-isolation by Schnöckel *et al.*[28] where chlorine and carbon monoxide were trapped in a solid argon matrix at 16 K. They observed vibrational frequencies at 1876.7 cm^{-1} (CO), 570.1 cm^{-1} (C···Cl) and 334.6 cm^{-1} (Cl···CO). Their *ab initio* calculations agreed with the experimental data obtained.

Dixon *et al.*[23] have conducted theoretical calculations on Cl···CO at the MP2 level (aug-cc-pVDZ) where they predicted a θ(O≡C···Cl) angle of 129.3°, a r(CO) bond length of 1.175 Å and the r(Cl···C) length as 1.810 Å. Results forthe Br···CO radical ($^2\Sigma^+$ state) were also obtained at the same level as this research and give almost identical data as detailed here (differences have been put in parentheses in Table 2). Romano *et al*. have conducted

matrix-IR experiments and have assigned a ν_{CO} vibration at 2045.7 cm^{-1}, which had been predicted previously by Dixon *et al*. to occur at 2082 cm^{-1}.

4.1. Optimised geometries

The $Cl^{-}\cdots CO$ and $Br^{-}\cdots CO$ cluster's optimised ground state geometry for the anion species were found to be strongly bent (L-shaped), in contrast to their neutral counterparts which were predicted to be linear, with ground state symmetry of $^{2}\Sigma^{+}$. Structural data can be found in Table 2, with cluster diagrams provided in Figure 21 & Figure 22.

The bond lengths r(C···X) calculated here are considered long and only weakly bound, whilst the r(CO) bond length is similar to that of free CO, reinforcing the weakly bound system.

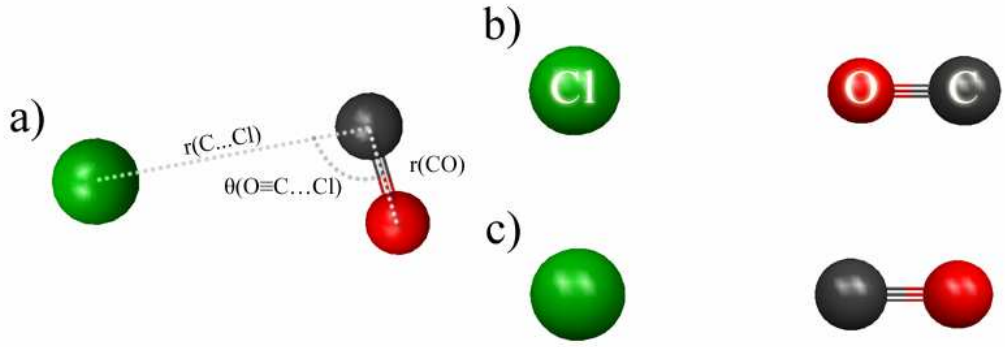

Figure 21 - The optimised geometry of the $Cl^{-}\cdots CO$ clusters: a) anion species and b) and c) the two neutral species.

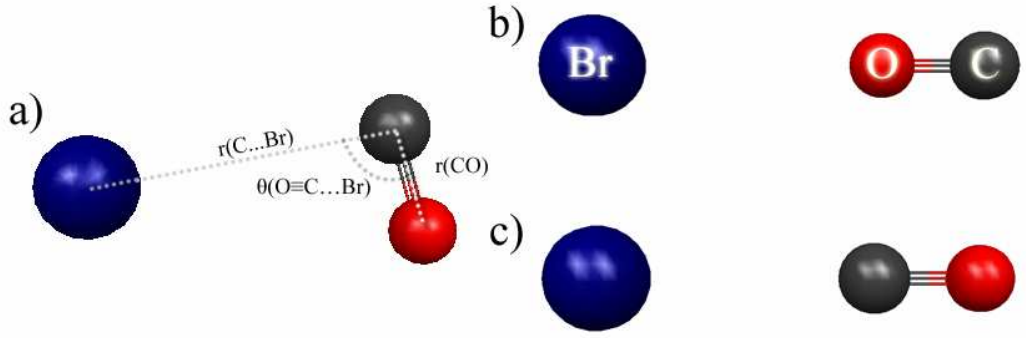

Figure 22 - The optimised geometry of the $Br^{-}\cdots CO$ clusters: a) anion species and b) and c) the two neutral species.

Table 2 – Calculated data for the minimum energy structures of the clusters $Cl^{-}\cdots CO$ and $Br^{-}\cdots CO$ and their constituents at MP2/aug-cc-pVDZ and MP2/aug-cc-pVTZ. Provided are the internal coordinates (r in Å and θ in degrees), harmonic vibrational frequencies (ω in cm^{-1}, symmetries included, intensities in km mol^{-1} in bold font style), zpe (in kcal mol^{-1}), MP2 energies (E_{MP2} in hartrees) and BSSE and zpe corrected energies (also in hartrees). Values in parentheses are differences to literature.[23]

Unit	CO		Cl^-		Br^-	
Theory level	pVDZ	pVTZ	pVDZ	pVTZ	pVDZ	pVTZ
r(C≡O)	1.150	1.139				
ω_1	2072 σ **34**	2110 σ **36**				
zpe	2.96	3.02				
E_{MP2}	-113.054970	-113.142411	-459.722765	-459.780792	-2572.609288	-2572.774831

Unit	$Cl^-\cdots CO$		Cl···CO		Cl···OC	
Theory level	pVDZ	pVTZ	pVDZ	pVTZ	pVDZ	pVTZ
r(C≡O)	1.153	1.142	1.149	1.138	1.150	1.139
r(C···Cl)	3.232	3.173	3.022	2.906		
r(O···Cl)					3.198	3.151
θ(O≡C···Cl)	95.1	95.2	180.0	180.0		
θ(C≡O···Cl)					180	180
ω_1	2056 *a′* **49**	2091 *a′* **52**	2081 σ **33**	2119 σ **34**	2071 σ **43**	2107 σ **45**
ω_2	134 *a′* **1**	137 *a′* **1**	70 σ **1**	68 σ **2**	50 π <**1**	57 σ <**1**
ω_3	83 *a′* **22**	83 *a′* **23**	49 π <**1**	58 π <**1**	26 π <**1**	26 π <**1**
ω_4			49 π <**1**	58 π <**1**	26 π <**1**	26 π <**1**
zpe	3.25	3.30	3.21	3.29	3.11	3.17
E_{MP2}	-572.782744	-572.928520	-572.649813	-572.792535	-572.648327	-572.790975
$E_{e/BSSE/Corr}$	-572.782016	-572.928102	-572.648730	-572.791779	-572.647897	-572.790588

Unit	$Br^-\cdots CO$		Br···CO		Br···OC	
Theory level	pVDZ	pVTZ	pVDZ[23]	pVTZ	pVDZ	pVTZ
r(C≡O)	1.152	1.141	1.149 (0)	1.138	1.151	1.139
r(C···Br)	3.444	3.383	3.128 (0)	2.979		
r(O···Br)					3.282	3.214
θ(O≡C···Br)	94.5	94.5	180.0 (0)	180.0		
θ(C≡O···Br)					180.0	180.0
ω_1	2059 *a′* **44**	2094 *a′* **47**	2082 (0) σ **35**	2120 σ **36**	2070 σ **45**	2107 σ **48**
ω_2	119 *a′* **1**	121 *a′* **1**	65 (0) σ **1**	69 σ **2**	49 π <**1**	54 σ <**1**
ω_3	67 *a′* **6**	66 *a′* **7**	47 (0) π <**1**	53 π <**1**	30π <**1**	30 π <**1**
ω_4			47 (0) π <**1**	53 π <**1**	30π <**1**	30 π <**1**
zpe	3.21	3.26	3.20	3.28	3.11	3.18
E_{MP2}	-2685.668869	-2685.922132	-2685.542617 (0.020038)	-2685.792748 (0.021743)	-2685.540929	-2685.790848
$E_{e/BSSE/Corr}$	-2685.667686	-2685.921254	-2685.540866	-2685.791071	-2685.539975	-2685.789932

4.2. 1D Potential energy slices

4.2.1. $\nu_{X\text{-}CO}$ stretch

For the $Cl^{-}\cdots CO$ clusters (both anion and neutral species) the $\nu_{Cl\text{-}CO}$ scan was undertaken by allowing the remaining two variables to relax (i.e. they were not constrained to their starting values). For the two other scans (i.e. ν_{CO} and $\theta_{Cl\text{-}CO}$) the two other variables not being scanned were 'fixed' to their optimised values for the entire vibrational mode.

Unfortunately the relaxed calculations for the $Br^{-}\cdots CO$ clusters proved to be difficult to perform and produced errors that were unable to be amended due to time constraints, and so all the results shown are for 'fixed' scans (see Table 2).

In each case the anion species shows the lowest energy in comparison to its neutral counterparts and has the deepest 'well' (largest D_E). This supports the idea that the closed shell of the anion is more stable than the open shell of the neutrals.

In Figure 23 the energy axis of both species extends 2000 cm^{-1} (1400 cm^{-1} for $Br^{-}\cdots CO$), although the neutrals (on the right scale) have been offset to 29000 cm^{-1} (28000 cm^{-1} for $Br^{-}\cdots CO$) so that they could be displayed together with the anion species.

It can be clearly seen that the anion species are far more stable in comparison to the neutral species. For both clusters the neutral species $X\cdots CO$ is the more stable of the two neutral species with a deeper well than $X\cdots OC$, but is still very shallow in contrast to the anion.

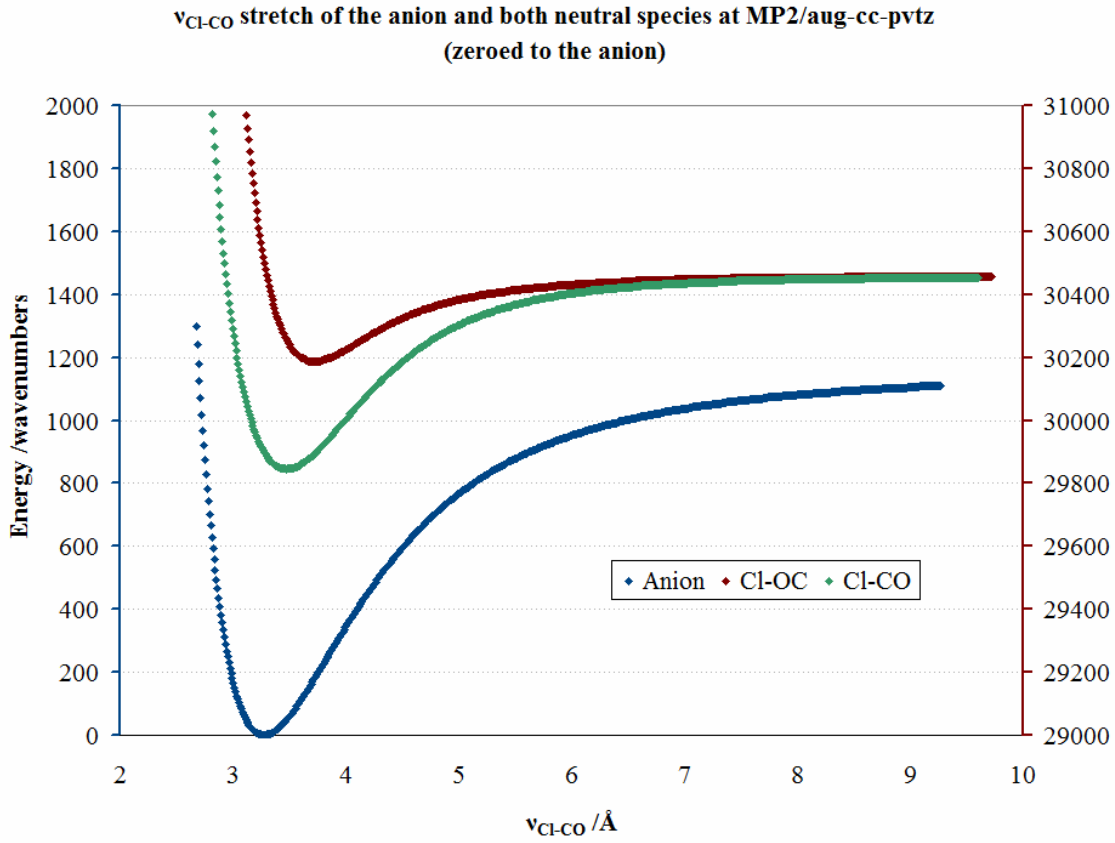

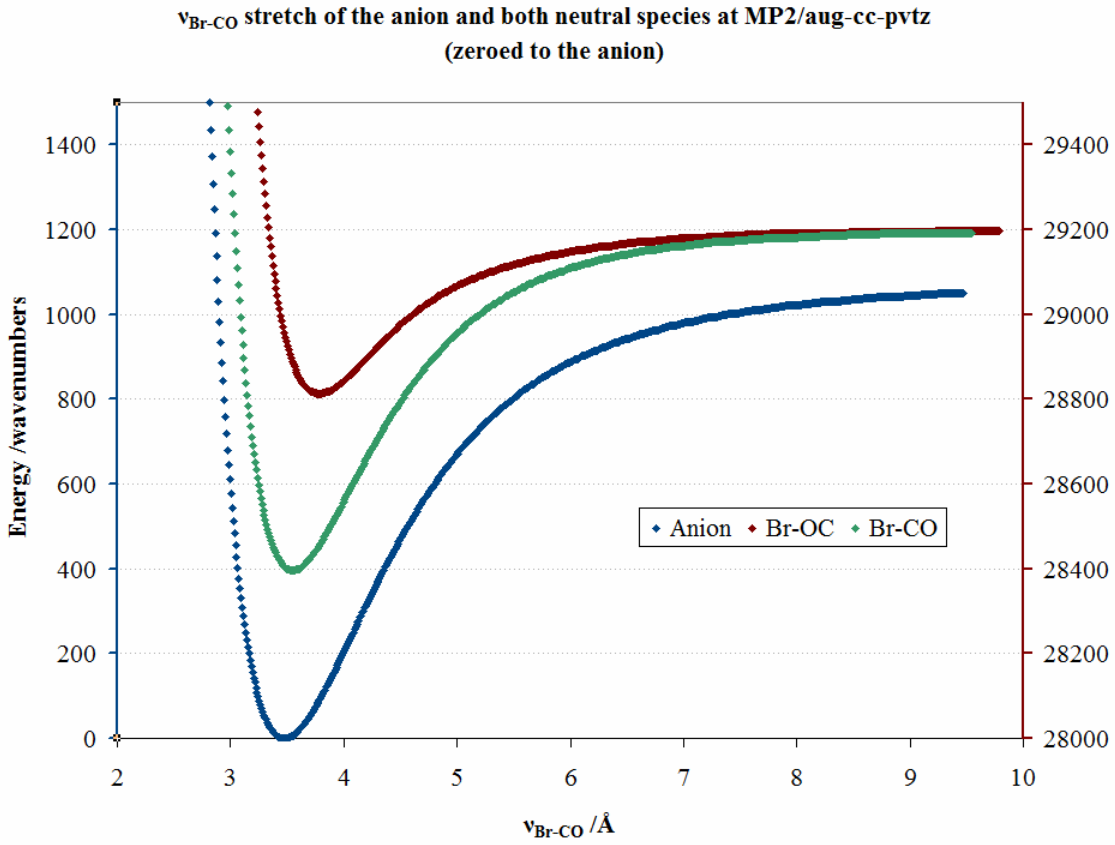

Figure 23 - The $\nu_{X\text{-}CO}$ stretch for X = Cl (top), Br (bottom). The neutral species (right scale on the y-axis) have been referenced to the anion (left scale).

4.2.2. ν_{CO} stretch

The ν_{CO} stretches for the X···OC neutral species exhibit an increase in slope at ~1.4 Å and a decrease at ~1.6 Å, eluding to another surface. This could be attributed to an ideal distance being reached between the oxygen and the halogen (due to dipole effects), as this is a scan where all the variables except the CO bond length have been set to the optimised values.

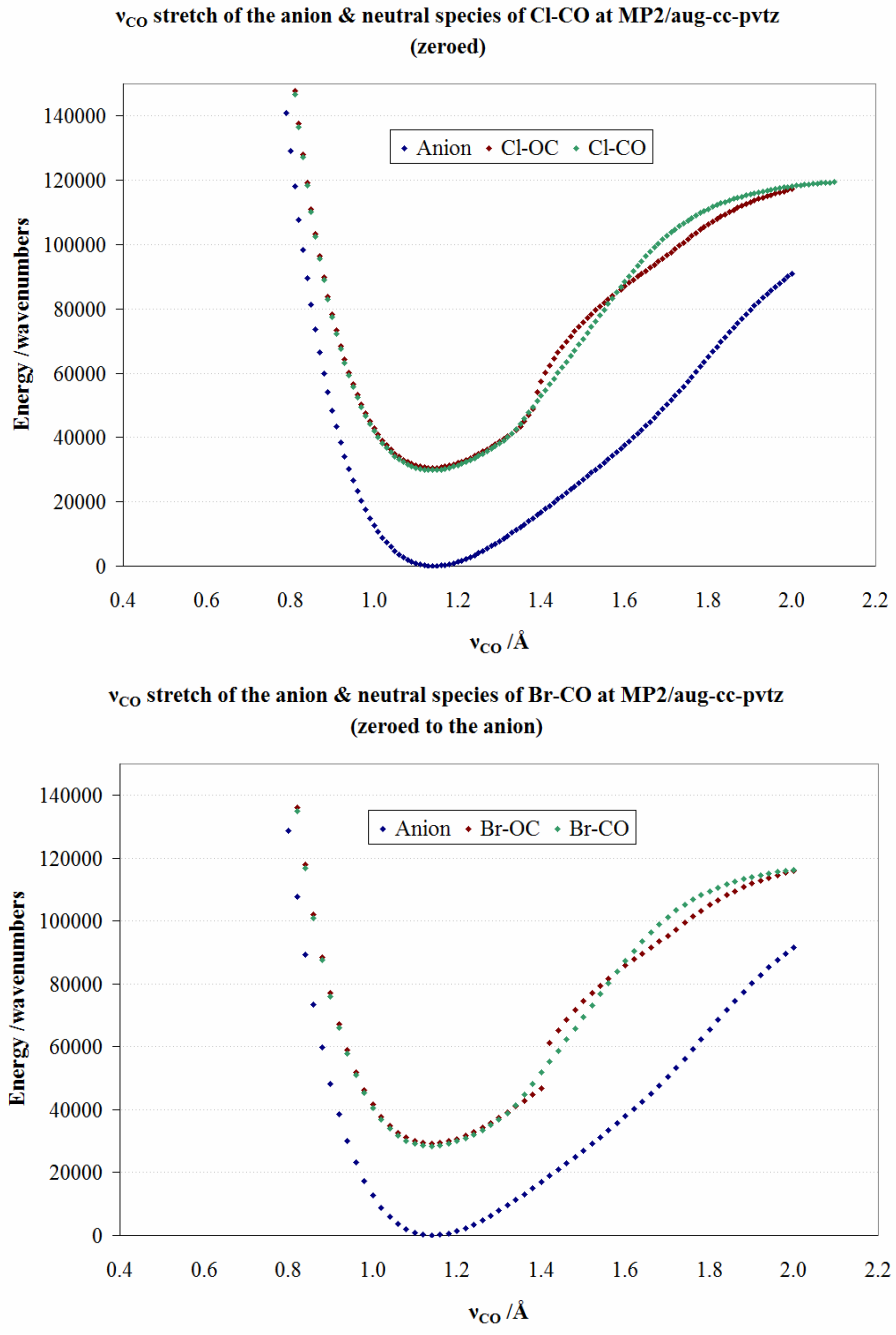

Figure 24 – A ν_{CO} stretch for Cl^{-}···CO (top) and Br^{-}···CO (bottom) clusters. The neutral species have been referenced to the anion's lowest energy.

4.2.3. $\theta_{X\text{-}CO}$ bend

For the bending mode the anion once again shows a deeper and narrower well compared to its' neutral counterparts. In Figure 25 the neutral species' energy scale is 600 cm^{-1}, whereas the anion's scale is ten times this. The difference in scales was carried out so that the depth of the neutrals' potential energy surfaces, as they appear almost flat otherwise, could be shown alongside the anion's surface. The difference in depths of the wells can now be easily viewed between the anion (approximately ten times greater) and neutral species.

The $Cl^{-\cdots}CO$ species has a double well which is attributed to the symmetry at 180° around the carbon monoxide. The anion is most stable when the halide is close to 75° (and 285°) to the centre of the carbon monoxide, corresponding to the angle $\theta(O{\equiv}C^{\cdots}X)$ in the optimised geometry.

At 0° the neutral is in the $X^{\cdots}CO$ configuration while at 180° the halogen has moved opposite and is now closest to the oxygen (i.e. in the other less stable neutral configuration: $X^{\cdots}OC$). The difference in energy between the two neutral scans can be accredited to the 1D potential energy scan's other variables remaining fixed. The distance between the halogen and the carbon monoxide during the scan, $r(X^{\cdots}OC)$, set to the calculated value for the optimised geometry of whichever neutral signifies a difference in the geometry between the two species and therefore in the energy at that geometry. If this variable were relaxed i.e. if the distance $r(X^{\cdots}OC)$ was not constrained (e.g. to 3.198 Å for the $Cl^{\cdots}OC$ neutral) then the energies for both neutral species would be expected to be identical.

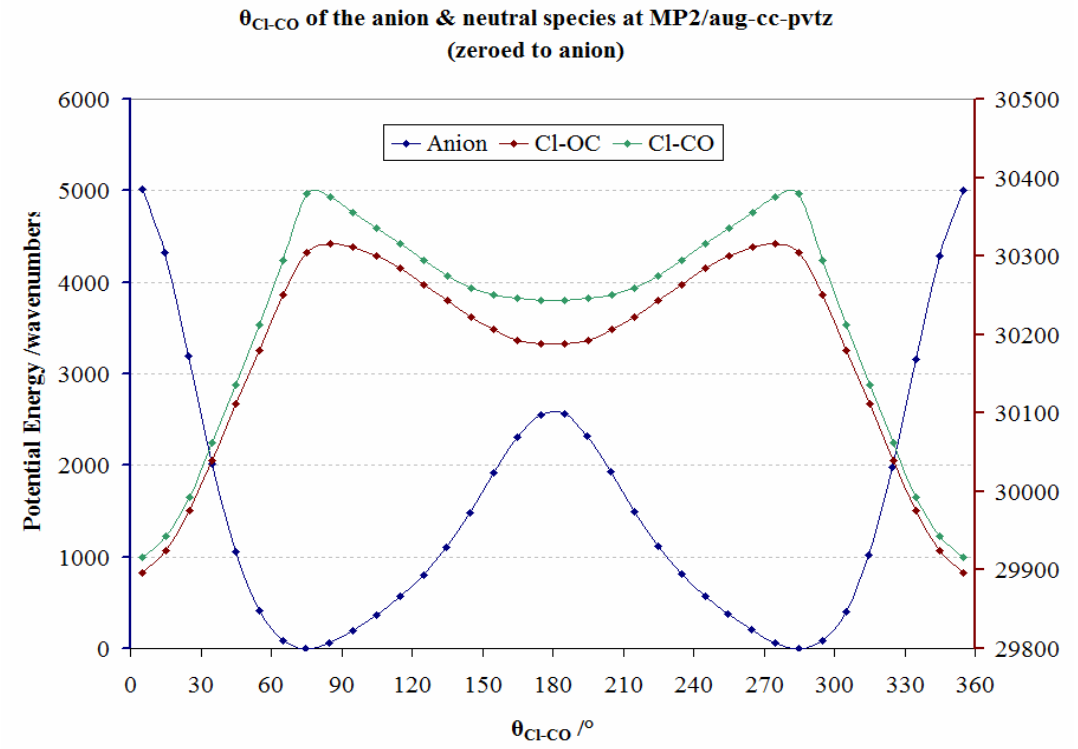

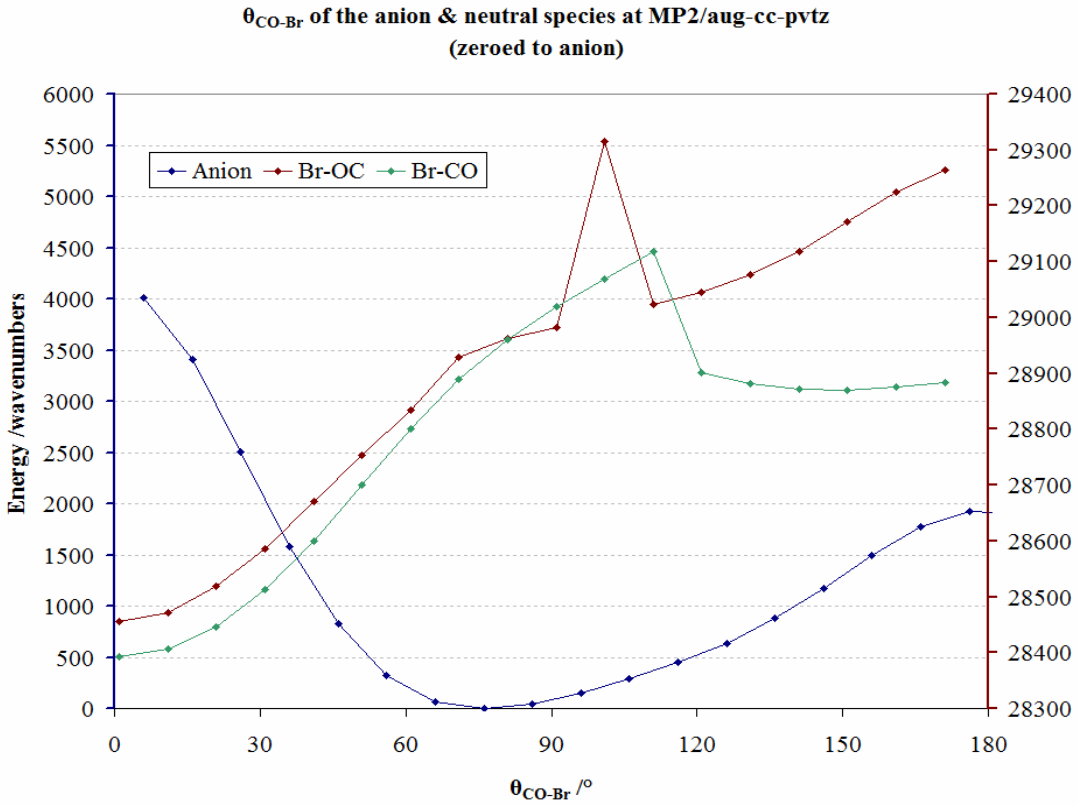

Figure 25 - A $\theta_{X\text{-}CO}$ bend. Both neutral species (right scale) have been referenced to the anion (left scale). For the $Cl^{-}\cdots CO$ cluster the surface is symmetric at 180° as it shows the same position but mirrored. For the $Br^{-}\cdots CO$ cluster both neutral species showed irregularities that require further investigation.

4.3. 2D Potential energy slices

The 1D potential energy scans do not show the complete potential energy surface experienced by the cluster during the vibrational modes. A 2D surface provides a better insight into the surface, although it would be preferable to envision the whole surface in its entirety if possible. Ultimately the more degrees of freedom a system has the more difficult it becomes to view the surface completely.

The potential energy surfaces of the neutral species for the 3D scans were difficult to obtain however a script (made by Dr. D. Wild, see Appendix 1) which could use either Gaussian 03/09 or GAMESS allowed the scans to continue even when a point on the surface could not be optimised. There were still some points on the surface that failed, but these were few in number compared to the total surface (~1%), and had greatly decreased compared to the amount of failed points encountered before the script was implemented. These new scans were compared to the previous work to check the points correlated, and this was the case.

For the 2D potential energy scans shown here (see Figure 26, Figure 27 and Figure 28) only two coordinates are varied (the intermolecular distance and angle), with the third axis displaying the energy. Although the scan was completed for all three vibrational modes (the corresponding data is found on the CD, a layout is detailed in Appendix 2), one of the variables (ν_{CO}) had to be maintained at a single value. The surfaces represented were chosen at the optimal r_{CO} distance for each computation (either 1.1 or 1.2 Å, which is close to the optimised distance calculated for the species, see Table 2). The neutral and anion of each cluster are depicted at the same CO distance. The energy of the neutral has, as for the 1D potential energy scans, been referenced to the anion's energy.

Both the $Br^{-}\cdots CO$ and $Cl^{-}\cdots CO$ clusters displayed artefacts in the neutral species, attributed to the low level of theory, as these are no longer visible for the pVTZ scan of $Cl^{-}\cdots CO$.

Unfortunately the $r_{Br...CO}$ stretch was not reduced to a small enough distance leaving the anion species with an incomplete surface, thus requiring further work.

Although the calculations for the 3D potential energy surfaces have been completed, a predicted spectrum using these surfaces could not be performed with the resources at hand. In the future it is hoped they can be processed using programs such as ezSpectrum[29], which will provide a predicted spectrum with more accuracy and precision than those from only 1D potential energy surfaces.

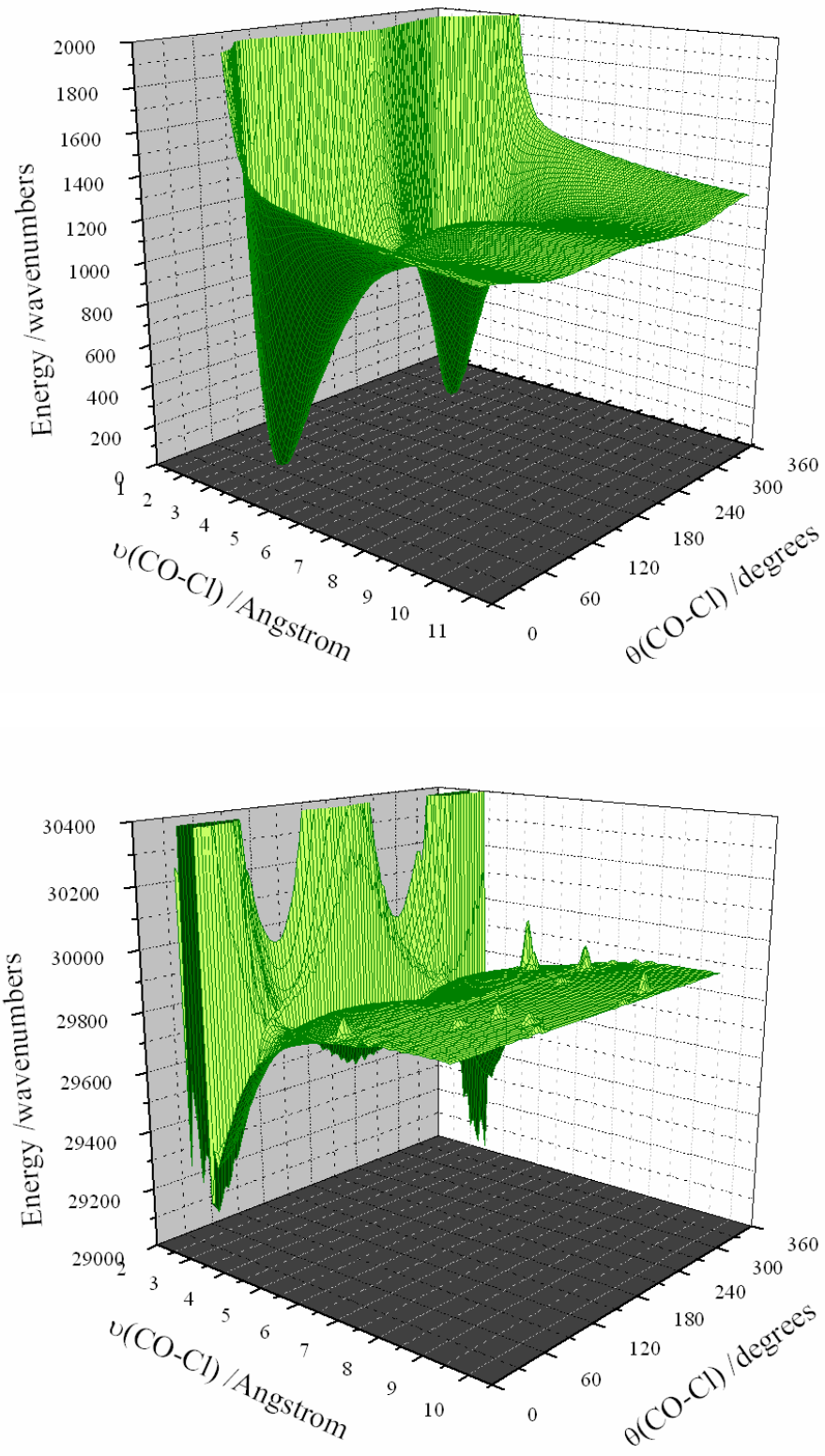

Figure 26 - A 'slice' of the 2D potential energy scan of the $Cl^{-}\cdots CO$ anion (top) and neutral (bottom). This slice was taken while maintaining a CO distance of 1.2 Å and scanning the $\nu_{Cl\text{-}CO}$ stretch and $\theta_{Cl\text{-}CO}$ bend.

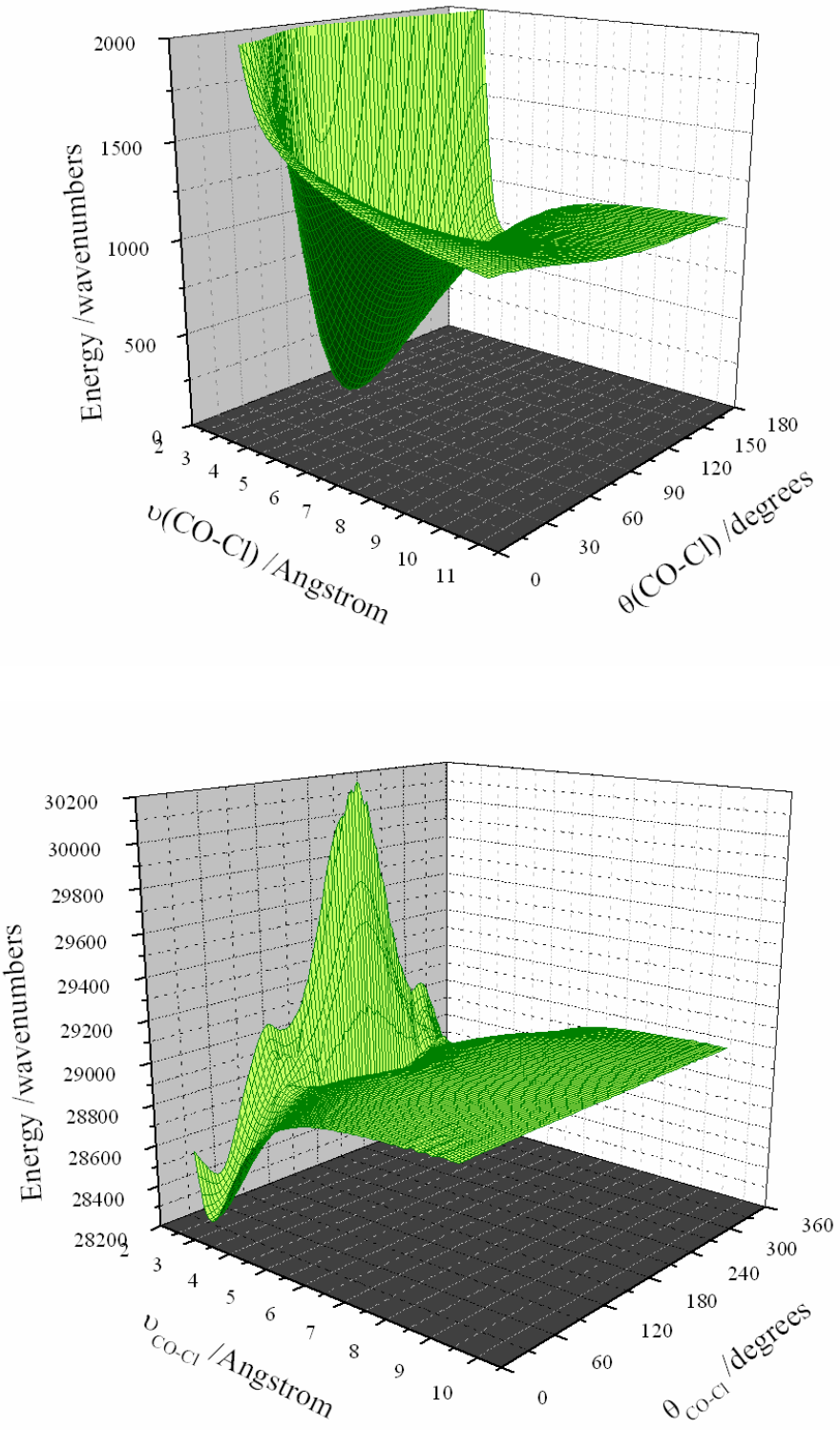

Figure 27 - A 'slice' of the 2D potential energy scan of the Cl-CO anion (top) and neutral (bottom) calculated at MP2/aug-cc-pvtz (in GAMESS [21] for the neutral). This slice was taken while maintaining a CO distance of 1.1 Å and scanning the $\nu_{Cl\text{-}CO}$ stretch and $\theta_{Cl\text{-}CO}$ bend. Note the angle only goes up to 180 degrees for the anion.

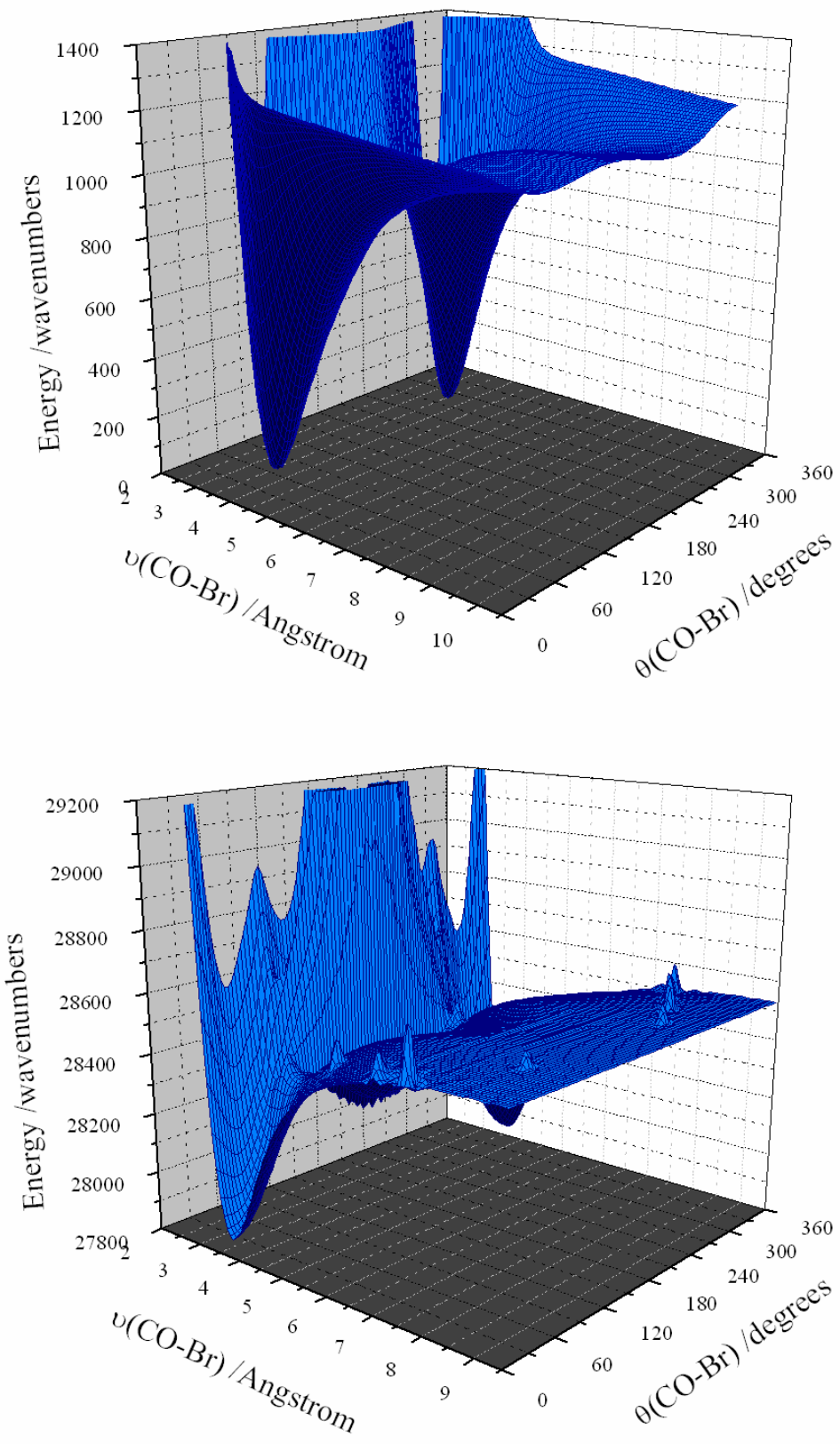

Figure 28 - A 'slice' of the 2D potential energy scan of the Br-CO anion (top) & neutral (bottom) species at MP2/aug-cc-pvdz. This slice was taken while maintaining a CO distance of 1.2 Å and scanning the $\nu_{Br\text{-}CO}$ stretch and $\theta_{Br\text{-}CO}$ bend.

4.3.1. Comparison with DFT methods

Another set of scans were computed using DFT theory for comparison and also to verify if DFT is more suited to producing the potential energy surfaces than MP2 for van der Waals clusters. In Figure 29 the 2D potential energy surfaces are shown using the M062X density functional (with the aug-cc-pVDZ basis set). This particular density functional was chosen because it has "excellent performance for main group chemistry, predicts accurate valence and Rydberg electronic excitation energies" and was recommended for use with "systems where main-group thermochemistry, kinetics, and noncovalent interactions are all important".[30] It should be noted that these scans only go up to 180° for the bend.

Regrettably the surface from the neutral species was not brought to a small enough distance for the $\nu_{Cl\text{-}CO}$ stretch as the inner wall does not extend high enough to form a complete well, still, where the MP2 scan showed artefacts, here there are none. However the surface along the asymptote is not as flat as the surface produced in the MP2 scan. In the future it may be worth investigating if these bulges are reduced in the pVTZ basis set. The anion surface is almost 1000 cm^{-1} lower than the one calculated at MP2, however the difference between the anion and neutral surfaces has increased by ~300 cm^{-1}.

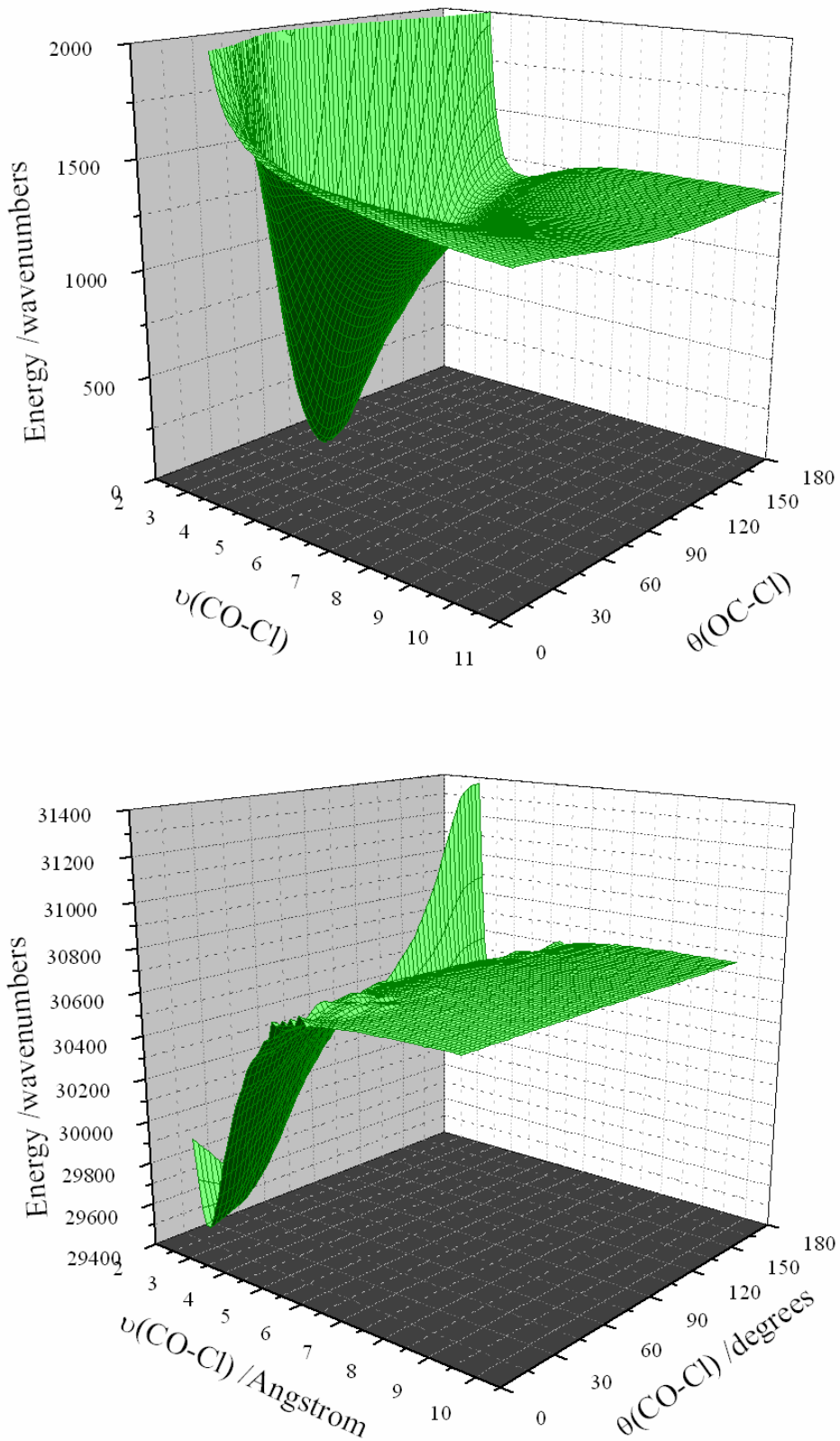

Figure 29 – A 'slice' of the 2D Potential energy surfaces of the $Cl^{-}\cdots CO$ anion (top) and neutral (bottom) species using the DFT basis set MO62X/aug-cc-pVDZ. The CO distance was frozen at 1.1 Å while scanning the $\nu_{Cl\text{-}CO}$ stretch and $\theta_{Cl\text{-}CO}$ bend. Note the angle only reaches 180 degrees.

4.4. Predicted spectra

For the 1D potential energy surfaces the program LEVEL 8.0 [22] is used to solve the radial Schrödinger equation (i.e. the $r_{X\text{-}CO}$ stretch) and then the Franck-Condon factors (or overlap integrals) for the probability of transitions between the anion and neutral surface and thus create a predicted spectrum. This predicted spectrum has been overlayed on the experimental data obtained in Figure 30 and Figure 31.

In the transition from anion to neutral afforded by the laser's energy, both the $Cl^{-}\cdots CO$ and $Br^{-}\cdots CO$ are launched onto the potential energy surface corresponding to the more stable of the two neutral configurations: $X\cdots CO$ (i.e. with the halogen adjacent to the carbon).

When looking at the predicted photoelectron spectra the important features to observe are the overall structure of the spectrum and which transition is most probable, as these should not change between basis sets or theory levels, whereas the energies at which the transitions occur do alter.

4.4.1. $Cl\cdots CO$

In Figure 30 the comparison between the $Cl\cdots CO$ predicted spectra calculated at pVDZ and pVTZ can be seen. Both basis sets predicted the most probable transition being the 0←0. For the hot band progression from the $\nu = 1$ vibrational level the most probable transition is also to the ground state (i.e. 0←1). These have been calculated for the $\nu_{Cl\text{-}CO}$ stretch in which variables have been relaxed.

The predicted spectra made from an identical stretch but with the variables kept restricted during the scan is in Appendix 3 for comparison. The only difference noted was a decrease in intensity of the probability of each transition.

The overall shape of the predicted spectra seem to agree visually with the experimental spectrum's, with a sharp edge on the right hand side (electrons with lower binding energies) and a trailing edge on the left hand side. The experimental spectrum does require

greater resolution before conclusive statements can be made as to whether the most probable transition predicted by *ab initio* calculations agrees with the experimental data.

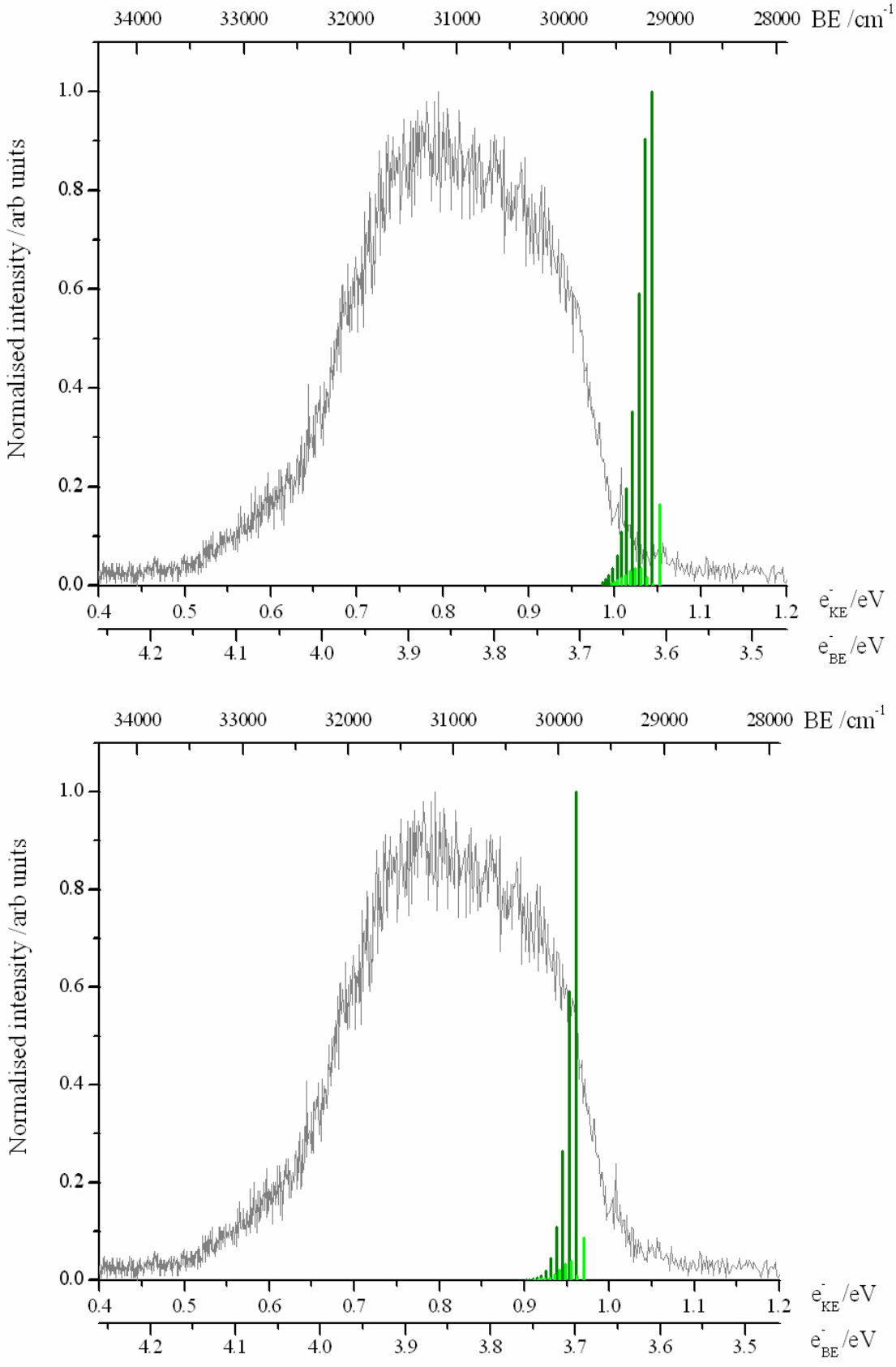

Figure 30 – Predicted spectra overlayed on the experimental spectrum obtained of Cl···CO. Both basis sets (top: pVDZ, bottom: pVTZ) predict the 0 ← 0 as the most probable transition. The bright green corresponds to hot band transitions from the v=1 vibrational level.

4.4.2. Br···CO

The same general shape of both the experimental and predicted spectrum can be seen for the Br···CO cluster (Figure 31). It should be noted that the predicted spectra for Br···CO used the 1D surface where the other variables were fixed to their optimised geometry in the $\nu_{Br\text{-}CO}$ stretch. Once again the most probable transition is the 0←0. For the hot band progression from the ν = 1 vibrational level the progression is 1←1 at pVDZ, but for pVTZ it changes to 0←1, the same as for the Cl···CO cluster. In fact for the pVTZ the 1←1 transition has about the same probability as the 1←0 transition. The intensity of the transitions has also greatly decreased from pVDZ to pVTZ, more so than Cl···CO.

As mentioned previously, the resolution of both experimental spectra need to be improved before any conclusive statements can be made as to whether the predicted spectra agree with the experimental data on the most probable transition occurring.

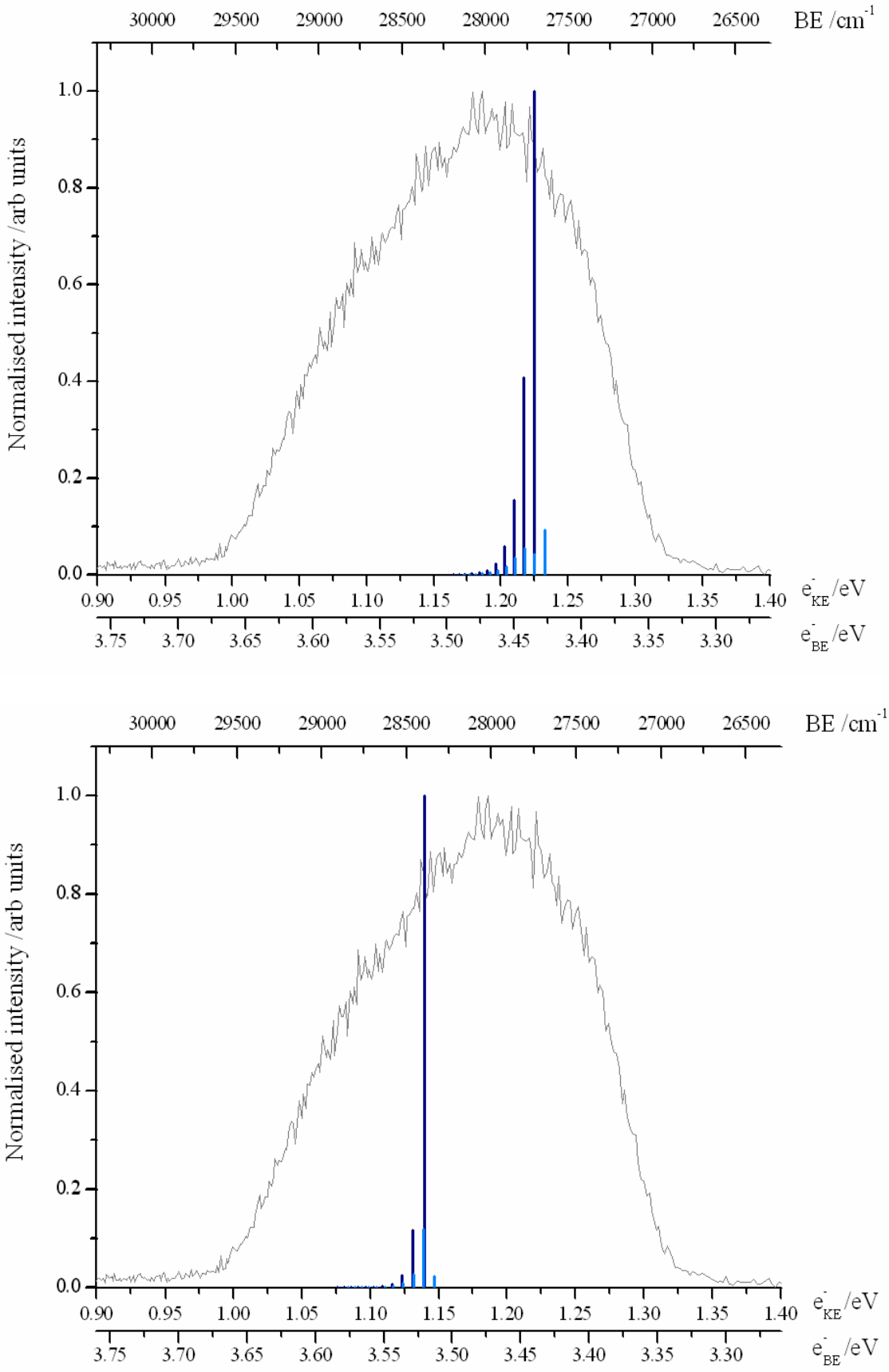

Figure 31 - Predicted spectra overlayed on the experimental spectrum obtained of Br¨CO. Both basis sets (top: pVDZ, bottom: pVTZ) predict the 0 ← 0 as the most probable transition. The bright blue corresponds to hot band transitions from the v=1 vibrational level.

5. Future work

Although in this work the study of the chloride and bromide clusters with carbon monoxide has been covered both theoretically and experimentally, there is still room for improvement. One such area that still requires work includes potential energy surfaces for the bromide clusters from scans with non-constrained variables and creating predicted spectra from these relaxed scans. These scans should also reduce the $r_{Br\text{-}CO}$ stretch to a smaller radius in order to create a complete surface. The level of theory used could always be increased (to pVQZ or greater), and work done by DFT methods could be employed for comparison.

It is hoped that the 3D potential energy surfaces which have been calculated already can be used for a vibrational overlap analysis with the program ezSpectrum[29] and the Franck-Condon factors should provide more precise spectra than those from 1D potential energy surfaces.

Experimentally there are also a number of improvements and further investigations that could be completed in the future. A preliminary effort was made to deduce which gas mixture composition increases the yield of clusters; however a more comprehensive study is necessary. This in turn could allow the opportunity to take photoelectron spectra of larger clusters (i.e. $X^{\cdot\cdot}(CO)_n$ where n = 2, 3, …) whose photoelectron spectra were previously too weak to be detected.

A great part of future work will involve improving resolution of the photoelectron spectra and a few propositions are being considered. The signal-to-noise ratio will hopefully increase by the addition of cone-shaped baffles with knife-edges (see Figure 11) both on the entrance and exit path of the laser, which will reduce backscatter. These baffles are currently being built and are expected to be installed shortly.

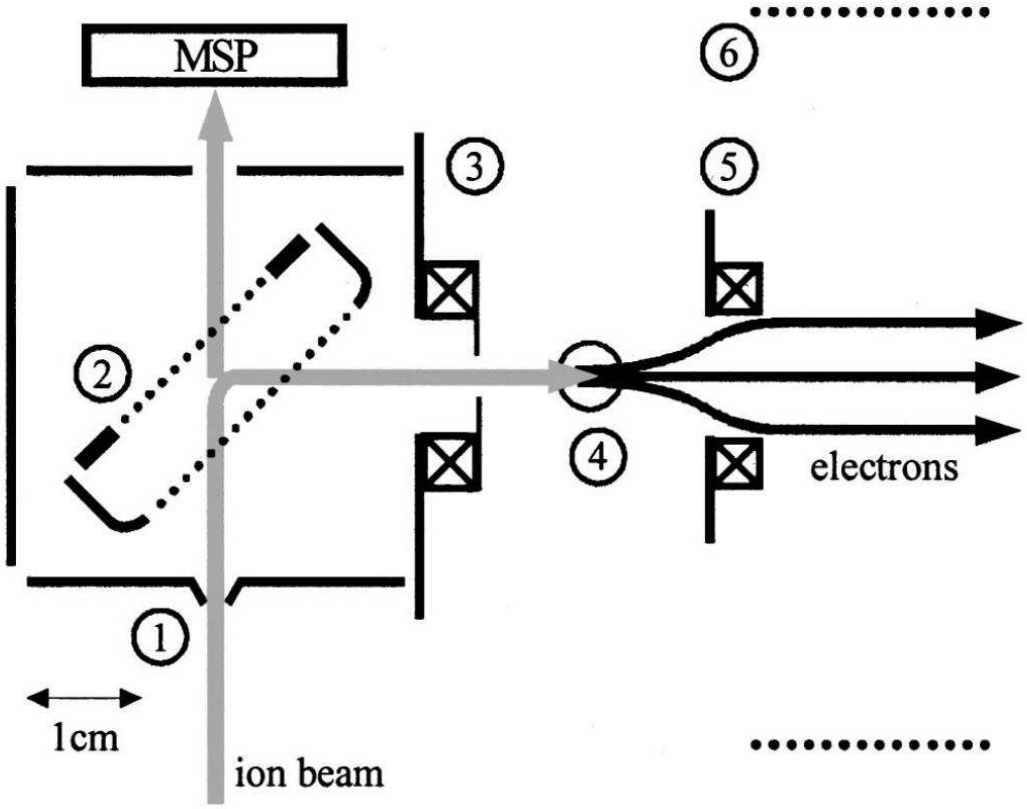

Figure 32 – Schematic showing how selected ions would be deflected using 99 % transmittant grids (region 2) with switched voltages and then have electrons photodetached (region 4). Taken from reference.[31]

A change in setup (see Figure 32) by deflecting the ions and then photodetaching is another possibility to give better resolution, as the photoelectrons would not have the additional velocity of the ions when being photodetached. This would require two grids with 99% transmittance allowing ions to pass through and be detected under normal conditions but can be switched to negative voltages to deflect the selected ion towards the photoelectron TOF tube. The laser beam would also require shifting towards the photoelectron TOF tube so it could then interact with the ions after they had been deviated.

For future spectra there is also the option of using a laser beam diameter of 3 mm, as the photoelectron spectra taken for this research were done solely with a laser beam of 6 mm. A decrease in beam diameter reduces the ionisation volume, which could improve resolution since the electrons will be initially spread over a smaller area (hence

experiencing more similar forces). To do this only lenses in the ‘telescope’ setup of the laser assembly need to be exchanged.

6. Conclusion

One year after the construction of the TOF-PES preliminary mass and photoelectron spectra from the clusters Cl···CO and Br···CO have been obtained. An intense, stable signal for both ions and photoelectrons has been made possible with modifications completed this year including reworked ion decelerator potentials, a rearranged laser setup, and knife edges on orifices in the extraction chamber and on baffle cones of the laser.

Preliminary photoelectron spectra of the van der Waals clusters Br···CO and Cl···CO have been recorded and reflect a similar structure to predicted spectra from *ab initio* calculations. Transitions between the ground state of the anion species to the ground state of the neutral species (i.e. 0←0) were predicted to be the most favoured for both clusters. Further work is required on creating potential energy surfaces and a predicted spectrum from the $^2A'$ electronic state of the neutral species for both Cl···CO and Br···CO. Prior to confirming any correlation between theory and experiment regarding the most favourable transition, the resolution of the experimental spectra must be enhanced.

7. Appendices

7.1. Appendix 1

A script created by Dr. D. Wild to be used with Gaussian 03/09, GAMESS or others to conduct continuous 3D scans, even if a point on the surface is not optimised.

```
#!/bin/bash
#PBS -j oe
#PBS -l walltime=17:00:00
#PBS -l ncpus=8:8
#PBS -l vmem=15GB
#PBS -l jobfs=2000MB
#PBS -l software=g03
#PBS -wd

module load gaussian/g03e01-fast

#!/bin/sh
#
# This script will perform potential energy scans using the Gaussian 03
# Programme
#
# It is preferred to using the internal G03 SCAN function as failure of
one
# scan point will not stop the script
#
#
# Give the scan job a title here
# The short title will form the name of the scan output file

title="Cl-CO neutral at ump2/aug-cc-pvdz"
short_title="ClCOneutpvdz.5"
#
# The next section is where the scan variables are set
#
# _start is the starting value of the variable
# _del is the step size (in degs or Angstrom)
# -steps is the number of steps for each variable
#
# First attempt at 3D PES scan of Cl...CO neutral at pvdz using Duncan's
script.
#
# X
# X  1 1.0
# C  2 var1  1 90.0
# O  2 var1  1 90.0  3 180.0 0
# Cl 2 var2  3 var3  1 180.0 0
#
var1_start=0.25
var1_del=0.05
var1_steps=10
var2_start=3.0
var2_del=0.1
var2_steps=65
var3_start=5.0
var3_del=10.0
var3_steps=35
#
# The next is the value of i,j, and k for the loops below. This is
needed if a restart is necessary
# Look to the $shortname.ijk output file for the last value of i,j, and
k and set these below
# If this is the first time the scan is run, then set all to 1
#
i_num=11
j_num=64
```

```
k_num=26
#
# The next part will change the number of steps so it is in line with
what
# is done with Gaussin 03 (i.e. do the first point, and then n steps
more)
# Comment these lines out if you have already accounted for this above
#
var1_steps=`expr $var1_steps + 1`
var2_steps=`expr $var2_steps + 1`
var3_steps=`expr $var3_steps + 1`
Succ=0
keymaster="# mp2/aug-cc-pvdz NoSymm Pop=None"         #  Put  your  Level
of theory keywords here
keywords=$keymaster
i_j_k=`expr $i_num + $j_num + $k_num`
if [ $i_j_k -gt 3 ]
    then
      keywords="$keywords Guess=Check "
fi
NumPoints=`echo "$var1_steps*$var2_steps*$var3_steps"|bc`
#
# Print some info to the .log and .ijk files
#
echo $title > $short_title.log
echo "This scan will produce $NumPoints values" >> $short_title.log
echo "VAR1  VAR2  VAR3  Energy" >> $short_title.log
echo "I     J     K" > $short_title.ijk
#
# Next comes the loops which will scan through the variables above
# More can be put in, you only need to increase the number of nested
loops
#
var1=`echo " (($i_num-1) * $var1_del) + $var1_start" | bc`
for (( i=$i_num; i<=$var1_steps; i++ ))
do
    var2=`echo " (($j_num-1) * $var2_del) + $var2_start" | bc`
    for (( j=$j_num; j<=$var2_steps;  j++ ))
    do
        var3=`echo " (($k_num-1) * $var3_del) + $var3_start" | bc`
        for (( k=$k_num; k<=$var3_steps; k++))
        do
          while [ $Succ -lt 1 ]
          do
                echo "%chk=temp.chk" > temp.inp
                echo "%mem=15GB" >> temp.inp
                echo "%nproc=8" >> temp.inp
                echo $keywords >> temp.inp
                echo "" >> temp.inp
                echo "Scan temp file" >> temp.inp
                echo "" >> temp.inp
                echo "0,2" >> temp.inp
                export z0="X"
                export z1="X 1 1.0"
                export z2="C 2 $var1 1 90.0"
                export z3="O 2 $var1 1 90.0 3 180.0 0"
                export z4="Cl 2 $var2 3 $var3 1 180.0 0"
                echo $z0 >> temp.inp
                echo $z1 >> temp.inp
                echo $z2 >> temp.inp
                echo $z3 >> temp.inp
                echo $z4 >> temp.inp
                echo ""  >> temp.inp

#
# The next section will start the programme, wait for completion and
# search for the energy value. If no value is found, then 3 other SCF
solving techniques
# are used. If after this, the SCF doesn't converge then "Fail" written
#
                g03 < temp.inp > temp.log 2>&1
                sleep 1
```

```
                En=`grep "EUMP2" temp.log | awk '{print $6}'`
                if [ -z $En ]
                  then
                      try=`expr $try + 1`
                    else
                      Succ=1
                fi
                if [ "$try" -eq "1" ]
                    then
                      keywords="$keymaster            SCF=(MaxCycle=1000)
Guess=Check "
                  elif [ "$try" -eq "2" ]
                  then
                      keywords="$keymaster         SCF=(QC,MaxCycle=1000)
Guess=Check "
                  elif [ "$try" -eq "3" ]
                  then
                      keywords="$keymaster        SCF=(XQC,MaxCycle=1000)
Guess=Check "
                  elif [ "$try" -gt "3" ]
                  then
                      En=Fail
                      Succ=1
                fi
          done
          echo "$var1   $var2 $var3 $En" >> $short_title.log
          echo "$i      $j    $k" >> $short_title.ijk
          rm temp.inp
          export keywords="$keymaster SCF=(MaxCycle=200) Guess=Check"
          try=0
          Succ=0
          var3=`echo "$var3 + $var3_del" | bc`
          k_num=1
        done
    var2=`echo "$var2 + $var2_del" | bc`
    j_num=1
    done
var1=`echo "$var1 + $var1_del" | bc`
done
echo "Scan finished!" >> $short_title.log
echo "Scan finished!" >> $short_title.ijk
#
# Clean up temporary files
#

rm temp.*
```

7.2. Appendix 2

Energies for 3D scans can be found in the Appendix folder on the CD provided with this thesis. Below is an image describing the layout of the CD.

7.3. Appendix 3

The predicted spectra of the Cl···CO cluster (Figure 33) with fixed coordinates in the $r_{Cl\text{-}CO}$ stretch (rather than relaxed as presented in this work).

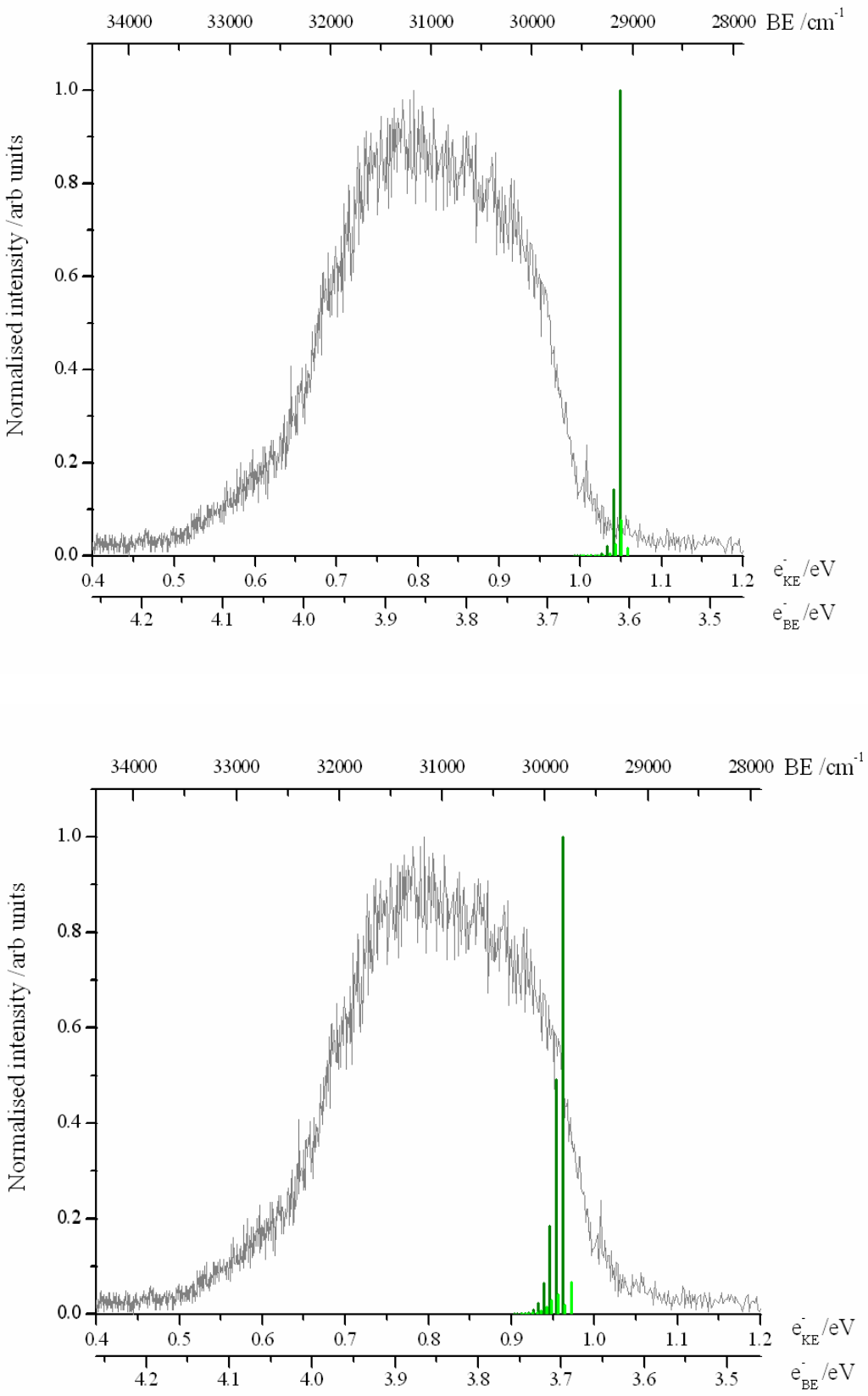

Figure 33 – Predicted spectra overlayed on the experimental spectrum obtained of Cl⋯CO. Derived from fixed coordinate stretch. Both basis sets (top: pVDZ, bottom: pVTZ) predict the 0 ← 0 as the most probable transition. The bright green corresponds to hot band transitions from the v=1 vibrational level.

7.4. Appendix 4

A script created to facilitate the extraction of energetic data from ‘relaxed’ scans conducted in Gaussian 03/09.

```
#!/bin/sh
#
# This script will extract data from relaxed scans performed in Gaussian
# and convert them to single column outputs.
#
# It is recommended that only the necessary data from the bottom of the
# output file from Gaussian be used in a separate text document, rather
# than the whole file.
#
#
# Titles of files used:

echo "What is the name of the original output file? Please include the
.txt "
read name1
echo "What is the name of the first variable used? "
read var1
echo "What is the name of the second variable used? "
read var2
echo "What is the name of the third variable used? "
read var3

# First the EIGENVALUES will be extracted, then each individual energy
# will be put to a new line, after which an extra line is removed.

grep "EIGEN" $name1 | awk '{print $3}' > temp1.txt;
sed 's/-/\n-/g' temp1.txt > temp2.txt;
sed '/^$/d' temp2.txt > ENERGY.txt;

# The other variables will then be extracted & inserted into the new
output
# in single columns.

grep -w "$var1" $name1 | awk '{OFS="\n"} {print $2, $3, $4, $5, $6}' >
VAR1.txt
grep -w "$var2" $name1 | awk '{OFS="\n"} {print $2, $3, $4, $5, $6}' >
VAR2.txt
grep -w "$var3" $name1 | awk '{OFS="\n"} {print $2, $3, $4, $5, $6}' >
VAR3.txt

# Removing the temporary files:

rm temp1.txt
rm temp2.txt

echo "Check ENERGY.txt, VAR1.txt, VAR2.txt & VAR3.txt for results";
```

8. References

(1) van Ommen, Ruud J.; Polik, W. F. Accessed from: *http://www.chem.hope.edu/%7Epolik/poster/poly9601.gif*. on **20/04/2009**.

(2) Wayne, R. P. *Chemistry of Atmospheres*, 3rd ed.; Oxford University Press: New York; 2000.

(3) Regents of the University of Michigan. Accessed from: *http://www.windows.ucar.edu/earth/images/profile.jpg*. on **06/05/2009**.

(4) Nicovich, J. M.; Kreutter, K. D.; Wine, P. H. *J. Chem. Phys*. **1990**, *92*, 3539-3544.

(5) Hewitt, A. D.; Brahan, K. M.; Boone, G. D.; Hewitt, S. A. *Int. J. Chem. Kinet.* **1996**, *28*, 763-771.

(6) Romano, R. M.; Della Vedova, C. O.; Downs, A. J.; Tobon , Y. A.; Willner, H. *Inorg. Chem.* **2005**, *44*, 3241-3248.

(7) Bridgeman, A. J. *Inorganica Chimica Acta*. **2001**, *321*, 27-41.

(8) Castleman Jr., A. W.; Bowen, K. H. *J. Phys. Chem*. **1996**, *100*, 12911-12944.

(9) Bacic, Z.; Miller, R. E. *J. Phys. Chem*. **1996**, *100*, 12945-12959.

(10) DePuy, C. H. *Int. J. Mass Spectrom.* **2000**, *200*, 79-96.

(11) Harrison, J. F. Accessed from: *http://www.cem.msu.edu/~harrison/cem483/pelec.gif*. on **20/03/2009**.

(12) Ellison, G. B. Accessed from: *http://www.colorado.edu/chem/ellison/img/PES_Fig1.gif*. on **13/03/2009**.

(13) Wiley, W. C.; McLaren, I. H. *Rev. Sci. Instrum.* **1955**, *26*, 1150-1157.

(14) Cheshnovsky, O.; Yang, S. H.; Pettiette, C. L.; Craycraft, M. J.; Smalley, R. E. *Rev. Sci. Instrum.* **1987**, *58*, 2131-2138.

(15) LaMacchia, R. University of Western Australia, (Honours Thesis). **2008**.

(16) Quak, H. University of Western Australia, (Honours Thesis). **2009**.

(17) Courtesy of Wild, D. A. **2008**.

(18) Dube, P.; Kiik, M. J.; Stoicheff, B. P. *J. Chem. Phys*. **1995**, *103*, 7708-7722.

(19) M. J. Frisch, G. W. Trucks, H. B. Schlegel, G. E. Scuseria, M. A. Robb, J. R. Cheeseman, J. A. Montgomery, Jr., T. Vreven, K. N. Kudin, J. C. Burant, J. M. Millam, S. S. Iyengar, J. Tomasi, V. Barone, B. Mennucci, M. Cossi, G. Scalmani, N. Rega, G. A. Petersson, H. Nakatsuji, M. Hada, M. Ehara, K. Toyota, R. Fukuda, J. Hasegawa, M. Ishida, T. Nakajima, Y. Honda, O. Kitao, H. Nakai, M. Klene, X. Li, J. E. Knox, H. P.

Hratchian, J. B. Cross, V. Bakken, C. Adamo, J. Jaramillo, R. Gomperts, R. E. Stratmann, O. Yazyev, A. J. Austin, R. Cammi, C. Pomelli, J. W. Ochterski, P. Y. Ayala, K. Morokuma, G. A. Voth, P. Salvador, J. J. Dannenberg, V. G. Zakrzewski, S. Dapprich, A. D. Daniels, M. C. Strain, O. Farkas, D. K. Malick, A. D. Rabuck, K. Raghavachari, J. B. Foresman, J. V. Ortiz, Q. Cui, A. G. Baboul, S. Clifford, J. Cioslowski, B. B. Stefanov, G. Liu, A. Liashenko, P. Piskorz, I. Komaromi, R. L. Martin, D. J. Fox, T. Keith, M. A. Al-Laham, C. Y. Peng, A. Nanayakkara, M. Challacombe, P. M. W. Gill, B. Johnson, W. Chen, M. W. Wong, C. Gonzalez, and J. A. Pople. *Gaussian 03*, Gaussian, Inc.: Wallingford CT, 2004.

(20) M. J. Frisch, G. W. Trucks, H. B. Schlegel, G. E. Scuseria, M. A. Robb, J. R. Cheeseman, G. Scalmani, V. Barone, B. Mennucci, G. A. Petersson, H. Nakatsuji, M. Caricato, X. Li, H. P. Hratchian, A. F. Izmaylov, J. Bloino, G. Zheng, J. L. Sonnenberg, M. Hada, M. Ehara, K. Toyota, R. Fukuda, J. Hasegawa, M. Ishida, T. Nakajima, Y. Honda, O. Kitao, H. Nakai, T. Vreven, J. A. Montgomery, Jr., J. E. Peralta, F. Ogliaro, M. Bearpark, J. J. Heyd, E. Brothers, K. N. Kudin, V. N. Staroverov, R. Kobayashi, J. Normand, K. Raghavachari, A. Rendell, J. C. Burant, S. S. Iyengar, J. Tomasi, M. Cossi, N. Rega, J. M. Millam, M. Klene, J. E. Knox, J. B. Cross, V. Bakken, C. Adamo, J. Jaramillo, R. Gomperts, R. E. Stratmann, O. Yazyev, A. J. Austin, R. Cammi, C. Pomelli, J. W. Ochterski, R. L. Martin, K. Morokuma, V. G. Zakrzewski, G. A. Voth, P. Salvador, J. J. Dannenberg, S. Dapprich, A. D. Daniels, O. Farkas, J. B. Foresman, J. V. Ortiz, J. Cioslowski, and D. J. Fox. *Gaussian 09*, Gaussian, Inc.: Wallingford CT, 2009.

(21) M.W.Schmidt, K.K.Baldridge, J.A.Boatz, S.T.Elbert, M.S.Gordon, J.H.Jensen, S.Koseki, N.Matsunaga, K.A.Nguyen, S.Su, T.L.Windus, M.Dupuis, J.A.Montgomery *J. Comput. Chem.* **1993**, *14*, 1347-1363.

(22) R. J. Le Roy *LEVEL 8.0: A Computer Program for Solving the Radial Schrodinger Equation for Bound and Quasibound Levels*, University of Waterloo Chemical Physics Research Report CP-663 (2007); see http://leroy.uwaterloo.ca/programs/ .

(23) Dixon, D. A.; Peterson, K. A.; Francisco, J. S. *J. Phys. Chem. A.* **2000**, *104*, 6227-6232.

(24) Somoza, M. M. Accessed from: *http://en.wikipedia.org/wiki/File:Franck-Condon-diagram.png*. on **09/05/2009**.

(25) Rienstra-Kiracofe, J. C.; Tschumper, G. S.; Schaefer III, H. F. *Chem. Rev.* **2002**, *102*, 231-282.

(26) Eland, J. H. D. *Photoelectron Spectroscopy*, 2nd ed.; Butterworth & Co Ltd: London; 1984.

(27) Jacox, M. E.; Milligan, D. E. *J. Chem. Phys.* **1965**, *43*, 866-870.

(28) Schnockel, H.; Eberlein, R. A.; Plitt, H. S. *J. Chem. Phys.* **1992**, *97*, 4-8.

(29) V.A. Mozhayskiy and A.I. Krylov, ezSpectrum. Availabe from: http://iopenshell.usc.edu/downloads

(30) Zhao, Y.; Truhlar, D. G. *Acc. Chem. Res.* **2008**, *41*, 157-167.

(31) Giniger, R.; Hippler, T.; Ronen, S.; Cheshnovsky, O. *Rev. Sci. Instr.* **2001**, *72*, 2543-2549.